

SIMULATIONS OF ELECTRON MAGNETOHYDRODYNAMIC TURBULENCE

JUNGYEON CHO^{1,2}

AND

A. LAZARIAN²*Draft version October 25, 2021*

ABSTRACT

We present numerical simulations of electron magnetohydrodynamic (EMHD) and electron reduced MHD (ERMHD) turbulence. Comparing scaling relations, we find that both EMHD and ERMHD turbulence show similar spectra and anisotropy. We develop new techniques to study anisotropy of EMHD turbulence. Our detailed study of anisotropy of EMHD turbulence supports our earlier result of $k_{\parallel} \propto k_{\perp}^{1/3}$ scaling, where k_{\parallel} and k_{\perp} are wavenumbers parallel and perpendicular to local direction of magnetic field, respectively. We find that the high-order statistics show a scaling that is similar to the She-Leveque scaling for incompressible hydrodynamic turbulence and different from that of incompressible MHD turbulence. We observe that the bispectra, which characterize the interaction of different scales within the turbulence cascade, are very different for EMHD and MHD turbulence. We show that both decaying and driven EMHD turbulence have the same statistical properties. We calculate the probability distribution functions (PDFs) of MHD and EMHD turbulence and compare them with those of interplanetary turbulence. We find that, as in the case of the solar wind, the PDFs of the increments of magnetic field strength in MHD and EMHD turbulence are well described by the Tsallis distribution. We discuss implications of our results for astrophysical situations, including the advection dominated accretion flows and magnetic reconnection.

Subject headings: MHD — turbulence — solar wind

1. INTRODUCTION

Turbulence at scales below the proton gyroradius is of great importance in many astrophysical applications. Such turbulence involving motions of electrons is essential for understanding the small-scale magnetic field dynamics of plasmas. It is also important for understanding of magnetic fields in the crust of a neutron star (Goldreich & Reisenegger 1992). This turbulence has been measured at by solar wind probes (Leamon et al. 1998).

The origin of the small-scale turbulence in a magnetized plasma is easy to understand if we think of what is happening with turbulent motions at small scales. When turbulence is driven on large scales, turbulence energy cascades down to smaller scales. The nature of magnetized turbulence from the outer scale to the proton gyroradius scale is relatively well known. Magnetized turbulence above the proton gyroradius can be described by the standard magnetohydrodynamics (MHD). As the name implies, the standard MHD treats the plasma as a single fluid. MHD turbulence can be decomposed into cascades of Alfvén, fast and slow modes (Goldreich & Sridhar 1995; Lithwick & Goldreich 2001; Cho & Lazarian 2002, 2003). While fast and slow modes get damped at larger scales, Alfvénic modes can cascade down to the proton gyroradius scale. Near and below the proton gyroradius scale, single-fluid description fails and we should take into account kinetic effects. Then what will happen to the Alfvén modes that reach the proton gyroradius scale?

Recent years, the nature of small-scale MHD turbulence in the solar wind has drawn interest from researchers (Howes et al. 2008a,b; Matthaeus, Servidio, & Dmitruk

2008; Saito et al. 2008; Gary, Saito, & Li 2008; Schekochihin et al. 2009; Dmitruk & Matthaeus 2006). In situ measurements of the solar wind show magnetic fluctuations over a broad range of frequencies. In the rest frame of the spacecrafts, the magnetic fluctuations show a broken power-law spectrum. For example, Leamon et al. (1999) reported that, at $\sim 0.2Hz$, the spectrum breaks from a $\nu^{-1.67}$ power-law to a $\nu^{-2.91}$ power-law. In general, the spectral break-point lies in the range $0.2Hz \lesssim \nu \lesssim 0.5Hz$ (see Saito et al. 2008). The $\nu^{-1.67}$ power-law at $\nu \gtrsim 0.2Hz$ seems to be relatively robust and represents inertial range of Alfvénic MHD turbulence. However, the power index for $\nu \gtrsim 0.5Hz$ seems to vary between -2 and -4 (Leamon et al. 1998; Smith et al. 2006). This range, characterized by a steeper power-law index, is termed “dispersion range” (Stawicki, Gary, & Li 2001), which is different from the dissipation range. The true dissipation scale of turbulence may lie at the end of the dispersion range. When we convert frequency to length scale, the broken power-law implies that the magnetic energy spectrum changes from a $k^{-1.67}$ inertial range spectrum to a steeper dispersion range spectrum, as we move from large scales to small scales. The transition from the inertial range to the dispersion range occurs near the proton gyro-scale ρ_i . (However, it is also possible that it occurs at the ion inertial scale $d_i = \rho_i/\sqrt{\beta_i}$, where β_i is the ion plasma β . See discussion in Schekochihin et al. 2009). The identity of the dispersion range turbulence is still under debate.

Small-scale magnetized turbulence also plays important roles in other astrophysical objects. Among them, the crust of neutron stars gives us useful insights on the electron MHD (EMHD) model of small-scale magnetized tur-

¹ Dept. of Astronomy and Space Science, Chungnam National Univ., Daejeon, Korea; cho@canopus.cnu.ac.kr

² Dept. of Astronomy, Univ. of Wisconsin, Madison, WI53706, USA; lazarian@astro.wisc.edu

bulence. In the crust of neutron stars, ions are virtually immobile and, thus, the ion gyroradius scale can be regarded as infinite. Therefore, turbulence in the crust should be similar to small-scale turbulence. Since ions are immobile, they provide a smooth charge background and electrons carry all the current, so that

$$\mathbf{v}_e = -\frac{\mathbf{J}}{n_e e} = -\frac{c}{4\pi n_e e} \nabla \times \mathbf{B}, \quad (1)$$

where \mathbf{v}_e is the electron velocity, \mathbf{J} is electric current density, \mathbf{B} is magnetic field, c is the speed of light, n_e is the electron number density, and e is the absolute value of the electric charge. Inserting this relation into the magnetic induction equation, we can obtain the EMHD equation

$$\frac{\partial \mathbf{B}}{\partial t} = -\frac{c}{4\pi n_e e} \nabla \times [(\nabla \times \mathbf{B}) \times \mathbf{B}] + \eta \nabla^2 \mathbf{B}, \quad (2)$$

where η is magnetic diffusivity (see Kingsep, Chukbar, & Yankov 1990 for details about EMHD). Goldreich & Reisenegger (1992) first showed that magnetized turbulence in the crust of neutron stars can be described by the EMHD equation. They discussed the properties of EMHD turbulence in neutron stars and argued that EMHD turbulence can enhance ohmic dissipation of magnetic field in isolated neutron stars (see also Cumming, Arras, & Zweibel 2004).

In this paper, we will focus on spectrum and anisotropy of EMHD turbulence. Earlier researchers convincingly showed that energy spectrum of EMHD turbulence is steeper than Kolmogorov's $k^{-5/3}$ spectrum (Biskamp, Schwarz, & Drake 1996; Biskamp et al. 1999; Ng et al. 2003). They found that the energy spectrum follows

$$E(k) \propto k^{-7/3}. \quad (3)$$

The steep energy spectrum can be explained by the following Kolmogorov-type argument (Biskamp et al. 1996). Suppose that the eddy interaction time for eddies of size l is the usual eddy turnover time $t_{cas,l} \sim l/v_l$. Since $\mathbf{v} \propto \nabla \times \mathbf{B}$ (Eq. [1]), this becomes $t_{cas,l} \propto l^2/b_l$. Combining this with the constancy of spectral energy cascade rate ($b_l^2/t_{cas,l} = \text{constant}$), one obtains $E(k) \propto k^{-7/3}$. Note that $E(k)$ and b_l are related by $kE(k) \sim b_l^2$. Since earlier researchers convincingly obtained the $k^{-7/3}$ spectrum, more focus is given to anisotropy of EMHD turbulence.

Cho & Lazarian (2004; hereinafter CL04) derived the expression for anisotropy

$$k_{\parallel} \propto k_{\perp}^{1/3} \quad (4)$$

where k_{\perp} and k_{\parallel} should be understood as wavenumbers parallel and perpendicular to the *local* magnetic field, the same way as parallel and perpendicular wavenumbers are understood in Goldreich-Sridhar (1995) model of MHD turbulence³. The expression (4), as we discuss in §3, follows from the application of the critical balance notion to the electron MHD cascade.

In this paper, we only consider strong EMHD turbulence. Discussions on weak EMHD turbulence can be found in Galtier & Bhattacharjee (2003) and Galtier (2006). In §2, we compare EMHD and recently proposed ERMHD (Schekochihin et al. 2009) formalisms. In §3, we discuss expected scaling relations of EMHD and ERMHD

turbulence. In §4, we describe our numerical methods. In §5, we compare EMHD and ERMHD turbulence. In the section we perform simulations in an elongated numerical box (786×256^2). In §6, we present detailed study of anisotropy from an EMHD simulation with 512^3 resolution. In §7, we present high-order statistics and bispectra of EMHD turbulence. In §8, we calculate the probability distribution functions (PDFs) and briefly compare them with the solar wind data. We give discussions in §9 and summary in §10.

2. EMHD AND ERMHD

Alfven modes are incompressible and thus less prone to collisionless damping (Barnes 1966; Kulsrud & Pearce 1969). Therefore, in the solar wind, it is generally accepted that Alfvenic turbulence provides a suitable description of fluid motions on scales larger than the proton gyroscale. The physics of strong Alfven turbulence is relatively well understood (see, e.g., Goldreich & Sridhar 1995)

However, turbulence on scales smaller than the proton gyroscale is not well understood. Nevertheless, there are several models for this small-scale turbulence. Here, we consider only fluid-like models of the small-scale turbulence. In particular, we consider Electron MHD (EMHD) model and Electron Reduced MHD (ERMHD) model. The former has been studied since 1990s (Kingsep et al. 1990; Biskamp et al. 1996) and the latter has been proposed only recently (Schekochihin et al. 2009). Both models can be derived from the generalized Ohm's law.

2.1. EMHD

EMHD can be viewed Hall MHD in the limit of $k\rho_i \gg 1$, where ρ_i is the ion gyroradius. Hall MHD equations are very similar to the standard MHD ones. But, there are also differences. The most important difference is that Hall MHD is based on the generalized Ohm's law

$$\mathbf{E} = -\frac{\mathbf{v}}{c} \times \mathbf{B} + \frac{\mathbf{J} \times \mathbf{B}}{n_e e c} + \frac{\mathbf{J}}{\sigma}, \quad (5)$$

while the standard MHD uses the 'standard' Ohm's law

$$\mathbf{E} = -\frac{\mathbf{v}}{c} \times \mathbf{B} + \frac{\mathbf{J}}{\sigma}. \quad (6)$$

Here, \mathbf{v} is fluid velocity, \mathbf{E} is electric field, and σ is conductivity. Compared with that of the standard MHD, the induction equation of Hall MHD has an extra term (the $\mathbf{J} \times \mathbf{B}$ term on the right-hand side):

$$\begin{aligned} \frac{\partial \mathbf{B}}{\partial t} &= -c \nabla \times \mathbf{E}, \\ &= \nabla \times (\mathbf{v} \times \mathbf{B}) - \nabla \times \frac{\mathbf{J} \times \mathbf{B}}{n_e e} + \frac{c^2}{4\pi\sigma} \nabla^2 \mathbf{B} \\ &= \nabla \times (\mathbf{v} \times \mathbf{B}) - \nabla \times \frac{c(\nabla \times \mathbf{B}) \times \mathbf{B}}{4\pi n_e e} + \eta \nabla^2 \mathbf{B}, \end{aligned} \quad (7)$$

where $\eta = c^2/(4\pi\sigma)$ and we use $\nabla \times \mathbf{B} = (4\pi/c)\mathbf{J}$.

When we normalize magnetic field to a velocity (i.e. $\mathbf{B}/\sqrt{4\pi\rho} = \mathbf{B}/\sqrt{4\pi n_i m_i} \rightarrow \mathbf{B}$, where n_i is the ion number density and m_i is the ion mass), Eq. (7) becomes

$$\frac{\partial \mathbf{B}}{\partial t} = \nabla \times (\mathbf{v} \times \mathbf{B}) - d_i \nabla \times [(\nabla \times \mathbf{B}) \times \mathbf{B}] + \eta \nabla^2 \mathbf{B}, \quad (\text{Hall MHD}) \quad (8)$$

³ A wavelet description would be more appropriate, as usual wavenumbers are defined in the *global* magnetic field frame. We keep this in mind, while using the traditional wavenumber notations.

where

$$d_i = \frac{c\sqrt{4\pi n_i m_i}}{4\pi n_e e} = \frac{c}{\sqrt{4\pi n_i (Ze)^2/m_i}} = \frac{c}{\omega_{pi}} = \frac{\rho_i}{\sqrt{\beta_i}}. \quad (9)$$

Here, ρ_i is the ion gyroradius, $Z = n_e/n_i = q_i/e$, and β_i is the ion plasma beta:

$$\beta_i = \frac{n_i k_B T}{B^2/8\pi}, \quad (10)$$

where k_B is the Boltzmann constant. The order of magnitude values of the first and the second terms on the right-hand side are

$$\nabla \times (\mathbf{v} \times \mathbf{B}) \sim b^2/l, \quad (11)$$

$$d_i \nabla \times [(\nabla \times \mathbf{B}) \times \mathbf{B}] \sim d_i b^2/l^2, \quad (12)$$

where l is the scale of interest and we assume $v \sim b$. Eq. (8) reduces to the standard MHD induction equation for $l \gg d_i$, while it reduces to the Electron MHD equation for $l \ll d_i$:

$$\frac{\partial \mathbf{B}}{\partial t} = -d_i \nabla \times [(\nabla \times \mathbf{B}) \times \mathbf{B}] + \eta \nabla^2 \mathbf{B}. \quad (\text{EMHD}) \quad (13)$$

In usual collisionless plasmas, transition from standard MHD to EMHD occurs at the ion inertial scale d_i . When ions are immobile and provide a homogeneous background, as in the crust of a neutron star, EMHD can be applicable even at the outer scale of turbulence, which can be larger than d_i defined by the first two expressions in Eq. (9). Note that anisotropy of turbulence (i.e. $k_\perp \gg k_\parallel$) at d_i (in usual plasmas) or on the energy injection scale (in case ions are immobile) is not a necessary condition for EMHD.

2.2. ERMHD

Schekochihin et al. (2009) first derived ERMHD from kinetic RMHD equations. They also gave derivation of ERMHD equations from the generalized Ohm's law. Therefore the starting point of ERMHD may be also the generalized Ohm's law and derivation of ERMHD is identical to the EMHD case up to Eq. (7) (see previous subsection). Note that the velocity \mathbf{v} in Eq. (7) denotes ion velocity \mathbf{v}_i and that RMHD, hence ERMHD, assumes anisotropy of turbulence (i.e. $k_\perp \gg k_\parallel$).

However, ERMHD assumes that the term

$$\nabla \times (\mathbf{v} \times \mathbf{B}) \approx -\mathbf{B} \nabla \cdot \mathbf{v} \quad (14)$$

in Eq. (7) may not be negligible in the limit of $k\rho_i \gg 1$. That is, ERMHD assumes $\mathbf{v}_i \approx 0$ in this limit, but $\nabla \cdot \mathbf{v}_i = \nabla \cdot \mathbf{v}_e \neq 0$ (see Schekochihin et al. 2009). Taking this into account, one can rewrite the magnetic induction equation as

$$\frac{\partial \mathbf{B}}{\partial t} = -\mathbf{B} \nabla \cdot \mathbf{v}_i - \frac{c}{4\pi n_e} \nabla \times [\mathbf{B} \cdot \nabla \mathbf{B}], \quad (15)$$

which becomes

$$\frac{\partial \mathbf{B}_\perp}{\partial t} = -\frac{c}{4\pi n_e} \nabla_\perp \times [\mathbf{B} \cdot \nabla \mathbf{B}_\parallel], \quad (16)$$

$$\frac{\partial \mathbf{B}_\parallel}{\partial t} = -\mathbf{B}_0 \nabla \cdot \mathbf{v}_i - \frac{c}{4\pi n_e} \nabla_\perp \times [\mathbf{B} \cdot \nabla \mathbf{B}_\perp], \quad (17)$$

where \mathbf{B}_\parallel and \mathbf{B}_\perp denote the components of magnetic field parallel and perpendicular to the mean field \mathbf{B}_0 , respectively (see Appendix A of this paper and Appendix C of Schekochihin et al. 2009). Here we drop the dissipation term for simplicity.

Finally, from the continuity equation and the assumption of pressure balance, we can rewrite the above equations as

$$\frac{\partial \mathbf{B}_\perp}{\partial t} = -\frac{c}{4\pi n_e} \nabla_\perp \times [\mathbf{B} \cdot \nabla \mathbf{B}_\parallel], \quad (18)$$

$$\frac{\partial \mathbf{B}_\parallel}{\partial t} = -\frac{\beta_i(1+Z/\tau)}{2+\beta_i(1+Z/\tau)} \frac{c}{4\pi n_e} \nabla_\perp \times [\mathbf{B} \cdot \nabla \mathbf{B}_\perp] \quad (19)$$

(see Eqs. [A8] and [A14]), which become

$$\frac{\partial}{\partial t} \frac{\tilde{\mathbf{b}}}{\sqrt{4\pi n_i m_i}} = \frac{-\rho_i}{\sqrt{\beta_i}} \sqrt{\alpha} \nabla_\perp \times \left(\frac{\mathbf{B}}{\sqrt{4\pi n_i m_i}} \cdot \nabla \frac{\tilde{\mathbf{b}}}{\sqrt{4\pi n_i m_i}} \right), \quad (20)$$

where

$$\mathbf{B} = \mathbf{B}_0 + \mathbf{b}, \quad (21)$$

$$\mathbf{b} = \mathbf{b}_\perp + b_\parallel \hat{\mathbf{z}}, \quad (22)$$

$$\tilde{\mathbf{b}} = \mathbf{b}_\perp + \sqrt{\frac{1}{\alpha}} b_\parallel \hat{\mathbf{z}}, \quad (23)$$

$$\alpha \equiv \frac{\beta_i(1+Z/\tau)}{2+\beta_i(1+Z/\tau)}. \quad (24)$$

Here, $\mathbf{B}_0 (= B_0 \hat{\mathbf{z}})$ is the mean magnetic field, $\hat{\mathbf{z}}$ is a unit vector along the direction of \mathbf{B}_0 , $Z = q_i/e$ ($e = |q_e|$) is the ion-to-electron charge ratio, $\tau = T_i/T_e$ is the temperature ratio, n_e is the average electron number density. The vector \mathbf{b}_\perp (in Fourier space) is parallel to $\hat{\mathbf{z}} \times \hat{\mathbf{k}}_\perp$, where $\hat{\mathbf{k}}_\perp = \mathbf{k}_\perp/k_\perp$. Therefore, in Fourier space $\tilde{\mathbf{b}}_{\mathbf{k}}$ lies in the plane spanned by $\hat{\mathbf{z}} \times \hat{\mathbf{k}}_\perp$ and $\hat{\mathbf{z}}$, which means $\tilde{\mathbf{b}}_{\mathbf{k}}$ is perpendicular to \mathbf{k}_\perp .

3. EXPECTED SCALING RELATIONS

In the presence of a strong mean magnetic field, turbulence energy tends to cascade in the direction perpendicular to the mean field. As a result, in Fourier space, modes with $k_\perp \gg k_\parallel$ are predominantly excited. In real space, characteristic scales parallel to the mean field (l_\parallel) tend to be larger than those perpendicular to it (l_\perp). This is referred to as anisotropy of turbulence.

In the case of *standard* MHD turbulence, this global anisotropy has been studied since early 1980s (Shebalin, Matthaeus, & Montgomery 1983). On the other hand, Goldreich & Sridhar (1995) showed that there exists a regime of turbulence in which a critical balance is maintained between wave motions (with timescale of $t_w \sim l_\parallel/V_A$) and hydrodynamic motions (with timescale of l_\perp/v_l). This is the so-called strong turbulence regime and they found a certain relation between k_\parallel and k_\perp , $k_\parallel \propto k_\perp^{2/3}$, in the regime. This scale-dependent anisotropy was numerically confirmed by Cho & Vishniac (2000) and Maron & Goldreich (2001). Cho & Vishniac (2000) showed that this scale-dependent anisotropy can be measured only in a *local* coordinate frame which is aligned with the *locally averaged* magnetic field direction. The necessity of using a local frame is due to the fact that eddies are aligned along the local mean magnetic field, rather than the global mean field \mathbf{B}_0 . We call this kind of anisotropy as *local* anisotropy.

In the case of *EMHD* turbulence, anisotropy has been studied only recently. Dastgeer et al. (2000) and Dastgeer & Zank (2003) numerically studied global anisotropy of 2D EMHD turbulence. On the other hand, Ng et al. (2003) numerically studied local anisotropy of 2D EMHD turbulence, but used second-order structure functions, the

limitation of which will be discussed in Section §6.3. In CL04, we studied anisotropy of 3D EMHD turbulence. In CL04, we for the first time found that critical balance between wave motions and hydrodynamic motions also holds true in EMHD turbulence and that anisotropy of EMHD, $k_{\parallel} \propto k_{\perp}^{1/3}$, is stronger than that of standard MHD turbulence.

Anisotropy of *ERMHD* is expected to be similar to that of EMHD (Schekochihin et al. 2009). This is understandable from Eq. (20). Note that $\mathbf{b} = \mathbf{b}_{\perp} + b_{\parallel}\hat{\mathbf{z}}$ and $\tilde{\mathbf{b}} = \mathbf{b}_{\perp} + \sqrt{1/\alpha}b_{\parallel}\hat{\mathbf{z}}$ in the equation. The factor α is less than or equal to 1. If we assume $b_{\perp} \sim \sqrt{1/\alpha}b_{\parallel}$, then the parallel (or z) component of true magnetic field b_{\parallel} is equal to $\sim \sqrt{\alpha}b_{\perp} \leq b_{\perp}$. If $\alpha \sim 1$ and, hence, $\mathbf{b} \sim \tilde{\mathbf{b}}$, then Eq. (20) becomes the usual EMHD equation. Therefore it is trivial to show that anisotropy of ERMHD is similar to that of EMHD. On the other hand, if $\alpha \ll 1$ and, hence, $\mathbf{b} = \mathbf{b}_{\perp} + \sqrt{\alpha}\tilde{\mathbf{b}}_{\parallel} \sim \mathbf{b}_{\perp}$, then the ERMHD equation becomes different from the EMHD equation. However, in general, the parallel component of \mathbf{b} does not contribute much to the term $\mathbf{B} \cdot \nabla\mathbf{b}$, because $b_{\parallel}\hat{\mathbf{z}} \cdot \nabla \sim b_{\parallel}k_{\parallel} \ll \mathbf{b}_{\perp} \cdot \nabla \sim b_{\perp}k_{\perp}$ in the presence of anisotropy, $k_{\parallel} \ll k_{\perp}$. This means that what matters for energy cascade is the perpendicular component of \mathbf{b} , which is not directly affected by the value of α . Therefore, even in case of $\alpha \ll 1$, we expect that anisotropy of ERMHD is similar to that of EMHD. However, this conjecture needs to be tested by numerical calculations.

4. NUMERICAL METHODS

As we described earlier, EMHD and ERMHD equations involve with time evolution of magnetic field only. Since magnetic field is divergence-free, we can use incompressible numerical schemes to solve the equations.

4.1. The EMHD code

We adopt a pseudospectral code to solve the normalized EMHD equation in a periodic box of size 2π :

$$\frac{\partial \mathbf{B}}{\partial t} = -\nabla \times [(\nabla \times \mathbf{B}) \times \mathbf{B}] + \eta' \nabla^2 \mathbf{B}, \quad (25)$$

where magnetic field, time, and length are normalized by a mean field B_0 , the whistler time $t_w = L^2(\omega_{pe}/c)^2/\Omega_e$ (Ω_e = electron gyro frequency), and a characteristic length scale L (see, for example, Galtier & Bhattacharjee 2003). The resistivity η' in equation (25) is dimensionless. The dispersion relation of a whistler waves in this normalized units is $\omega = k k_{\parallel} B_0$. The magnetic field consists of the uniform background field and a fluctuating field: $\mathbf{B} = \mathbf{B}_0 + \mathbf{b}$. The strength of the uniform background field, B_0 , is set to 1. We use up to 512^3 collocation points. At $t = 0$, the random magnetic field is restricted to the range $2 \leq k < 5$ in wavevector space. The amplitudes of the random magnetic field at $t = 0$ is ~ 1.2 . In order to have a more extended inertial range, we use hyperdiffusivity for the diffusion terms⁴. The power of hyperdiffusivity is set to 3 for

⁴ We do not observe a strong bottleneck effect, which is a common feature in numerical hydrodynamic simulations with hyperviscosity/hyperdiffusivity. Therefore expect that hyperdiffusivity does not substantially alter physics in the inertial range. However, this should be clarified in the future. Discussions on the bottleneck effect for 2-dimensional EMHD can be found in Biskamp, Schwarz, & Celani (1998).

⁵ Or, equivalently, we may use $k_{\parallel} = 1, 2, 3, \dots$ and $k_{\perp} = 3, 6, 9, \dots$. In this case, the size of the computational box is $(2\pi/3) \times (2\pi/3) \times (2\pi)$, where 2π is the side along the mean magnetic field.

all simulations, so that the dissipation term in the above equation is replaced with $\eta_3(\nabla^2)^3\mathbf{B}$. We perform both driven and decaying turbulence simulations.

4.2. The ERMHD Code

The ERMHD equation is only slightly different from the EMHD equation. Therefore, we also adopt a pseudospectral code to solve the normalized ERMHD equation in a rectangular periodic box of size $2\pi \times 2\pi \times 6\pi$:

$$\frac{\partial \tilde{\mathbf{B}}}{\partial t} = -\nabla_{\perp} \times (\mathbf{B} \cdot \nabla \tilde{\mathbf{B}}) + \eta' \nabla^2 \tilde{\mathbf{B}}, \quad (26)$$

where

$$\tilde{\mathbf{B}} \equiv \mathbf{B}_0 + \tilde{\mathbf{b}}, \quad (27)$$

$$\tilde{\mathbf{b}} = \mathbf{b}_{\perp} + \sqrt{\frac{1}{\alpha}}b_{\parallel}\hat{\mathbf{z}}, \quad (28)$$

$$\tilde{t} \equiv \sqrt{\alpha}t, \quad (29)$$

where η' is dimensionless resistivity, \mathbf{b}_{\perp} and $b_{\parallel}\hat{\mathbf{z}}$ are perpendicular and parallel components of magnetic field, respectively, and definition of α is given in Eq. (24). Note that the ERMHD equation is very similar to the EMHD equation. Numerical setup is therefore similar to that of the EMHD case, except the shape of the simulation box.

We use an elongated numerical box for ERMHD to satisfy the condition $k_{\perp} \gg k_{\parallel}$. The numerical box is 3 times longer in the direction of the mean magnetic field. The wavenumbers along the mean field direction have fractional values

$$k_{\parallel} = 1/3, 2/3, 1, 4/3, \dots, \quad (30)$$

while those of perpendicular direction have integer values⁵. We perform only decaying turbulence simulations. At $t=0$, Fourier modes with $1/3 \leq k_{\parallel} \leq 1$ and $4.5/\sqrt{2} \leq k_{\perp} \leq 4.5\sqrt{2}$ are excited. The strength of the mean magnetic field (B_0) is 1 and the rms value of the random magnetic field (actually \tilde{b}) at $t=0$ is ~ 0.071 . Therefore, the critical balance, $b k_{\perp}/B_0 k_{\parallel} = 1$, is roughly satisfied at $t=0$. For comparison, we perform a similar EMHD simulation (Run E256D-EL).

5. RESULTS: EMHD AND ERMHD

We compare EMHD and ERMHD turbulence in Fig. 1. Left panel of Fig. 1 shows time evolution and energy spectra of decaying EMHD and ERMHD runs (see Runs E256D-EL, ER256D1-EL, and ER256D8-EL in Table 1). The inset shows time evolution of magnetic energy density. The solid curve is for ERMHD with $\sqrt{\alpha} = 1$, dotted curve for ERMHD with $\sqrt{\alpha} = 1/8$, and the dashed curve for EMHD. The horizontal axis represents time multiplied by $\sqrt{\alpha}$ and the vertical axis twice the magnetic energy density. In case of ERMHD with $\sqrt{\alpha} = 1/8$ (i.e. Run ER256D8-EL), the vertical axis is not b^2 , but $\tilde{b}^2 = b_{\perp}^2 + b_{\parallel}^2/\alpha$. All three curves follow a similar decay law. The main plot of Fig. 1 shows energy spectra at $\sqrt{\alpha}t = 0.6$ (see the arrow in the inset). All three spectra are consistent with the expected $k^{-7/3}$ spectrum.

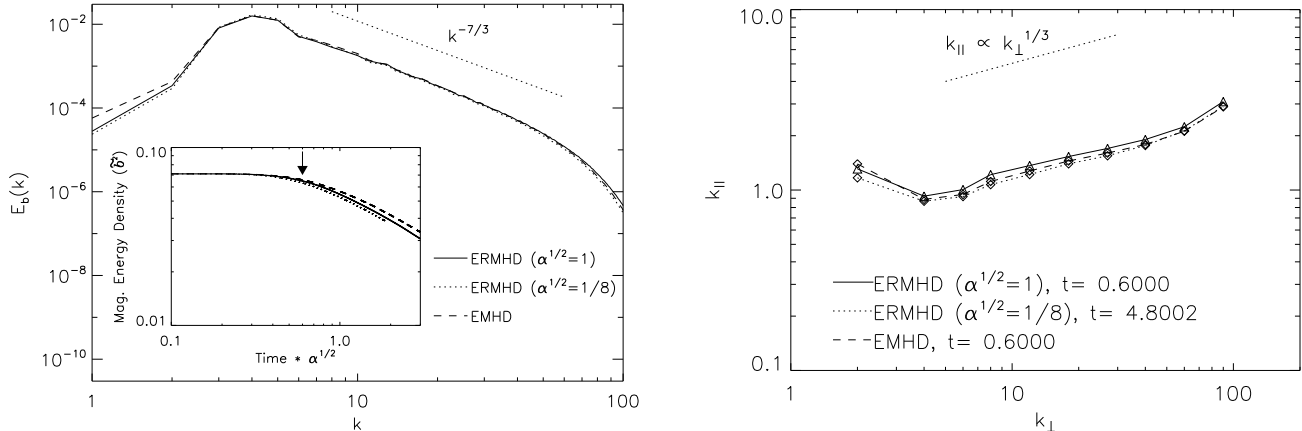


FIG. 1.— Comparison of EMHD (Run E256D-EL) and ERMHD (Runs ER256D1-EL and ER256D8-EL). *Left*: energy spectra and time evolution of magnetic energy density (inset). The energy spectra are taken at the time marked by the arrow in the inset. Note that the horizontal axis of the inset is $\sqrt{\alpha}t$, where α is a parameter that appears in the ERMHD formalism (Eq. [24]). The vertical axis of the inset is b^2 (or, in case of ER256D8-EL, \tilde{b}^2). *Right*: comparison of anisotropy. The calculations are done at the time marked by the arrow in the inset of left panel.

We compare anisotropy of EMHD and ERMHD in right panel of Fig. 1. We obtain the plot at $\sqrt{\alpha}t = 0.6$. All three curves show similar scaling relations, $k_{\parallel} \propto k_{\perp}^{1/3}$. Note however that, although we do not show it in this paper, anisotropy tends to get stronger as turbulence decays further. We will describe the method of obtaining anisotropy and its limitations in Section §6.1.

To summarize, we observe that both EMHD and ERMHD turbulence exhibit similar spectra and anisotropy. Spectra and time evolution of magnetic energy density of ERMHD turbulence seem to be invariant under the following transformation,

$$\mathbf{B} \rightarrow \tilde{\mathbf{B}}, \quad t \rightarrow \sqrt{\alpha}t. \quad (31)$$

6. RESULTS: SCALING OF EMHD

In the previous section, we have studied turbulence in a rectangular box elongated along the mean field direction. Note that the numerical resolution in the perpendicular direction is 256×256 , which limits the inertial range of turbulence. To increase the inertial range we need to increase numerical resolution in the perpendicular direction. Studying ERMHD is more difficult than studying EMHD because we need to use an elongated numerical box for ERMHD to satisfy the condition $k_{\perp} \gg k_{\parallel}$. For EMHD, there is no necessity of using such an elongated numerical box. Therefore, EMHD is more suitable for high resolution simulations. Since EMHD turbulence and ERMHD turbulence exhibit similar scaling relations, we only consider a high resolution EMHD simulation in this section.

We perform a decaying EMHD simulation with 512^3 grid points (Run E512D in Table 1). At $t=0$, Fourier modes with $2 \leq k < 5$ are excited. Here $k = \sqrt{k_{\perp}^2 + k_{\parallel}^2}$ and, thus, the initial perturbation is isotropic (i.e. $k_{\parallel} \sim k_{\perp}$). The strength of the mean magnetic field (B_0) is 1 and the rms value of the random magnetic field (b) is 1.21. Therefore, the critical balance, $bk_{\perp}/B_0k_{\parallel} = 1$, is roughly satisfied at $t=0$.

In this section, we focus on anisotropy of EMHD turbu-

lence. CL04 showed that anisotropy of EMHD turbulence is consistent with $k_{\parallel} \propto k_{\perp}^{1/3}$. However, since it is difficult to measure anisotropy of EMHD turbulence, more careful assessments of anisotropy are necessary. In this subsection, we develop and test new techniques for anisotropy. We analyze anisotropy of turbulence after turbulence has developed a full inertial range.

The energy spectra in left panel of Figure 2 show how the inertial range develops. At $t = 0$ only large-scale (i.e. small k) Fourier modes are excited. The dashed curve in Figure 2 shows the initial spectrum. As the turbulence decays, the initial energy cascades down to small scales and, as a result, small scale (i.e. large k) modes are excited. When the energy reaches the dissipation scale at $k \gtrsim 100$, the energy spectrum goes down without changing its slope (the dotted and the solid curves). The slope at this stage is very close to that of the predicted spectrum:

$$E(k) \propto k^{-7/3}. \quad (32)$$

For the study of anisotropy, we use the data cube at $t \approx 0.46$. The solid curve in left panel of Figure 2 represents the spectrum at that time.

The right panel of Figure 2 shows spectra of electric field. Both the total electric field (solid curve) and its xy-component (dashed curve) show spectra compatible with $k^{-1/3}$. (Note that we assume $\mathbf{B}_0 = B_0\hat{\mathbf{z}}$.) This result is consistent with the ones obtained by gyrokinetic simulations (Howes et al. 2008a) and Hall MHD simulations (see Dmitruk & Matthaeus 2006; Matthaeus et al. 2008). Bale et al. (2005) reported a similar electric fluctuation spectrum in the solar wind.

6.1. Anisotropy: method 1

In CL04, we noted that the quantity $\mathbf{B}_L \cdot \nabla \mathbf{b}_l$ is proportional to $B_L k_{\parallel} b_l$, where \mathbf{B}_L is the local mean field, \mathbf{b}_l the fluctuating field at scale l , and k_{\parallel} the wave number parallel to the local mean magnetic field. We obtained \mathbf{B}_L by eliminating Fourier modes whose perpendicular wavenumber is greater than $k/2$. We obtained the fluctuating field \mathbf{b}_l by

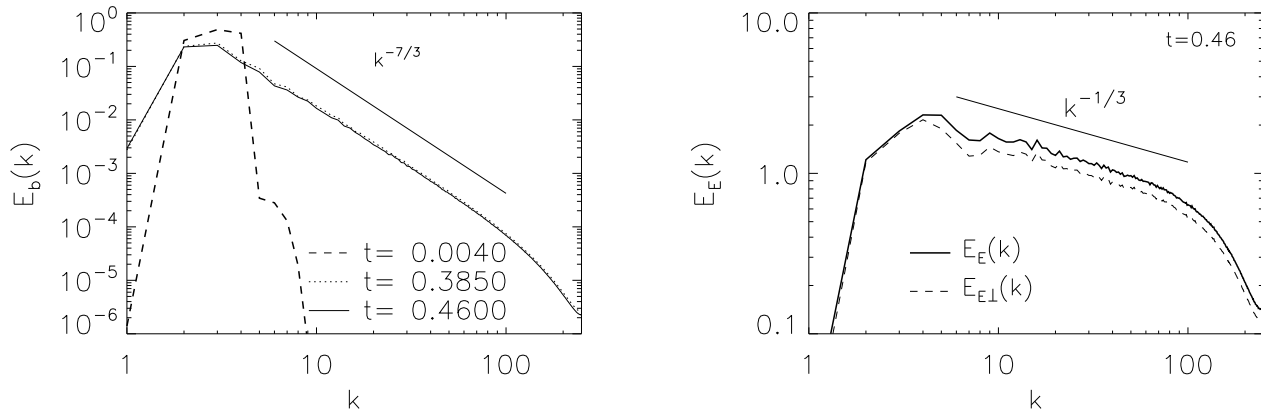


FIG. 2.— Spectra of \mathbf{B} (left) and \mathbf{E} (right) of EMHD turbulence (Run E512D). *Left*: spectrum at different time points. At $t \approx 0$, only small-wavenumber Fourier modes are excited. At later times, energy gradually cascades down to small scales (i.e. large k regions) and a $k^{-7/3}$ inertial range develops. *Right*: spectrum of electric field \mathbf{E} at $t=0.46$. The solid curve is the spectrum of total electric field and the dashed curve is that of electric field perpendicular to the mean field \mathbf{B}_0 .

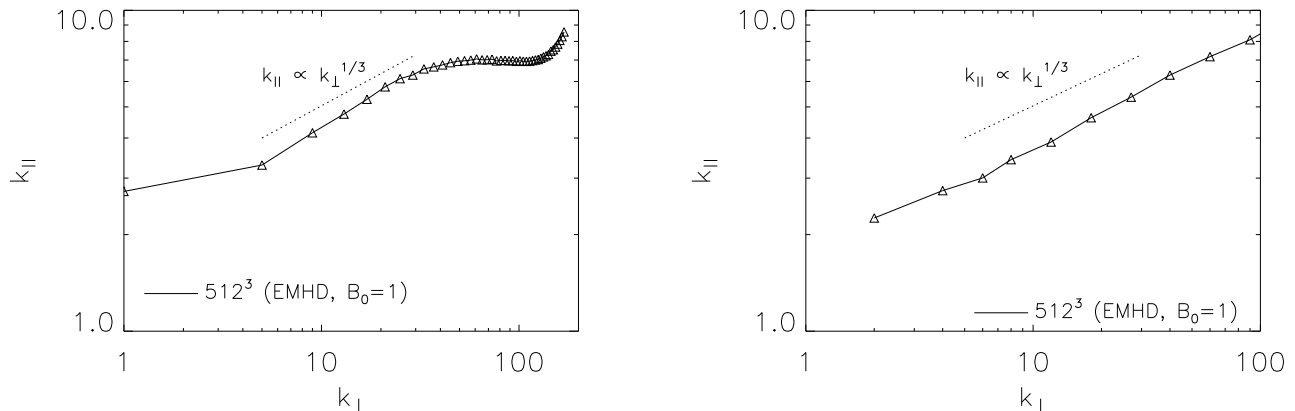


FIG. 3.— Anisotropy of EMHD turbulence (Run E512D). *Left*: the old method (Eq. [33]) is used. *Right*: a new method (Eq. [34]) is used.

eliminating Fourier modes whose perpendicular wavenumber is less than $k/2$. In CL04, we calculated anisotropy in Fourier space:

$$k_{\parallel}(k_{\perp}) \approx \left(\frac{\sum_{k \leq |\mathbf{k}'| < k+1} |\widehat{\mathbf{B}_L \cdot \nabla \mathbf{b}_l}|_{\mathbf{k}'}^2}{B_L^2 \sum_{k \leq |\mathbf{k}'| < k+1} |\widehat{\mathbf{b}}_{\mathbf{k}'}|^2} \right)^{1/2}. \quad (33)$$

The reason why we did the calculation in Fourier space is that there might be unknown contamination from scales other than l . We plot anisotropy obtained this way in left panel of Fig. 3.

We note that, when we obtain the fluctuating field \mathbf{b}_l by filtering out Fourier modes whose perpendicular wavenumber is less than $k/2$ or greater than $2k$, we may calculate anisotropy directly in real space:

$$\mathbf{B}_L \cdot \nabla \mathbf{b}_l \approx B_L k_{\parallel} b_l \rightarrow k_{\parallel} \approx \left(\frac{\langle |\mathbf{B}_L \cdot \nabla \mathbf{b}_l|^2 \rangle}{B_L^2 b_l^2} \right)^{1/2}. \quad (34)$$

We plot anisotropy obtained this way in right panel of Fig. 3. The result is compatible with the expected anisotropy, $k_{\parallel} \propto k_{\perp}^{1/3}$. The limitation of this method is

that the choice of the filtering wavenumbers, $k/2$ and $2k$, is an arbitrary one. When we use filtering wavenumbers of $k/\sqrt{2}$ and $\sqrt{2}k$, we get a slightly weaker anisotropy.

6.2. Anisotropy: method 2

In the previous subsection, we assumed that $\mathbf{B}_L \cdot \nabla \mathbf{b}_l \propto B_L k_{\parallel} b_l$. Is this really correct? If small-scale eddies are aligned with local mean field, the above assumption should be true. However, if the major axes of small-scale eddies are substantially misaligned with local large-scale mean field, the quantity $\mathbf{B}_L \cdot \nabla \mathbf{b}_l$ may sample perpendicular wavenumber of the eddies. In this subsection, we investigate alignment of small-scale eddies with respect to local mean magnetic field.

We first visualize the alignment effect. Left panel of Fig. 4 shows a snapshot of magnetic field structure in a plane parallel to the *global* mean magnetic field. The global mean magnetic field is parallel to the horizontal axis in the Figure. The white lines in Figure represent local mean magnetic field. We obtain the local mean field by filtering out Fourier modes with $k > 15$. The contours represent magnetic energy density of small-scale field. We

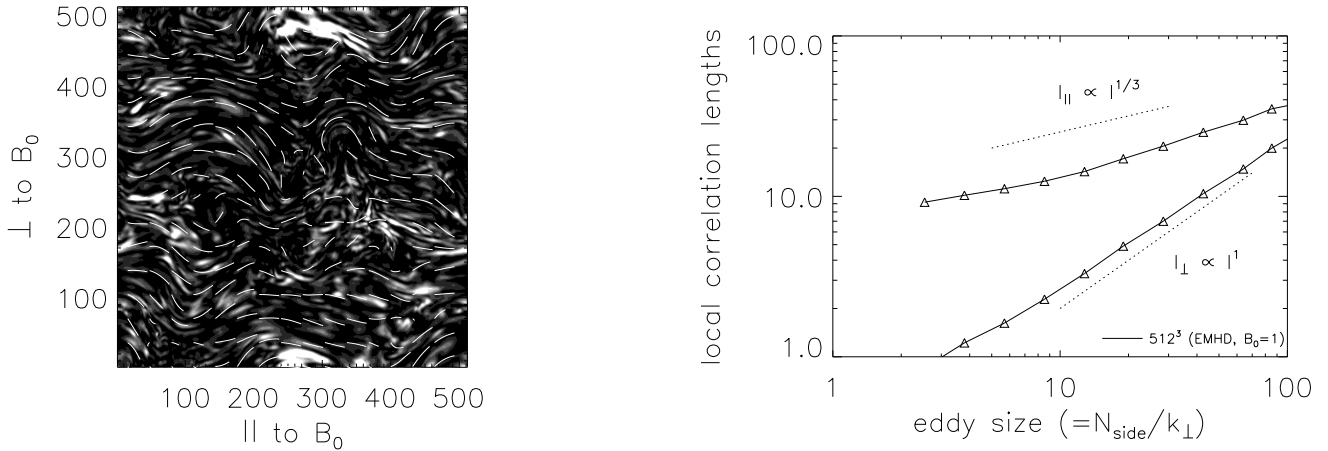


FIG. 4.— Anisotropy based on local correlation lengths (Run E512D). *Left*: visualization. White lines denote *local* mean magnetic field \mathbf{B}_L obtained by filtering out large- k Fourier modes. Contours show structure of small-scale eddies obtained by retaining Fourier modes near the scale of interest and filtering out all other scale Fourier modes. The global mean field \mathbf{B}_0 is parallel to the horizontal axis. *Right*: a new method based on correlation lengths in local frame. The parallel correlation length l_{\parallel} , for example, is the average of the correlation length measured along the local mean magnetic field direction at each point. (Note that the local mean magnetic field directions are marked by white lines in the left panel). In Run E512D, $N_{side} = 512$.

obtain the small-scale field by filtering out Fourier modes with $k \leq 15$ or $k \geq 60$. Since the alignment effect, if any, should be 3-dimensional effect in nature, we may not be able to visualize the effect correctly in a 2-dimensional plane. Nevertheless, we can observe that small-scale eddies are well aligned with the local mean field directions.

If small-scale eddies are well aligned with the local mean field, the correlation length along the local mean field should be larger than that of perpendicular directions. Furthermore, when the alignment effect is present, the parallel correlation length should follow a $l_{\perp}^{1/3}$ (or, $k_{\perp}^{-1/3}$) power law. We investigate the behavior of parallel and perpendicular correlation lengths by changing the scale l .⁶ We define the correlation lengths as the distances at which the 2-point correlation function $\langle \mathbf{b}_l(\mathbf{r}_1) \cdot \mathbf{b}_l(\mathbf{r}_2) \rangle$ drops by 50%. The parallel correlation length is measured along the directions of local mean field, \mathbf{B}_L , and the perpendicular one for perpendicular directions. In right panel of Fig. 4, we plot the parallel and perpendicular correlation lengths as functions of small-scale eddy size $l \propto 1/k$. The parallel correlation lengths (upper curve) is of course longer than the perpendicular ones (lower curve). On average, the parallel correlation lengths seem to follow the expected $l^{1/3}$ scaling. However, the slope is shallower than $1/3$ for small-size eddies and steeper than $1/3$ for large-size eddies. Roughly speaking, the perpendicular correlation lengths follow l^1 scaling, which is reasonable.

All in all, although it may not be not a perfect method, the filtering method reasonably reveals anisotropy of EMHD turbulence. The anisotropy of EMHD turbulence revealed by the filtering process is consistent with the $k_{\parallel} \propto k_{\perp}^{1/3}$ scaling.

6.3. Anisotropy: Multi-point second-order structure functions

We may visualize scale-dependent anisotropy using the second-order structure function calculated in the local frame, which is aligned with local mean magnetic field \mathbf{B}_L :

$$SF_2(r_{\parallel}, r_{\perp}) = \langle |\mathbf{B}(\mathbf{x} + \mathbf{r}) - \mathbf{B}(\mathbf{x})|^2 \rangle_{avg. \text{ over } \mathbf{x}}, \quad (35)$$

where $\mathbf{r} = r_{\parallel} \hat{\mathbf{r}}_{\parallel} + r_{\perp} \hat{\mathbf{r}}_{\perp}$. The vectors $\hat{\mathbf{r}}_{\parallel}$ and $\hat{\mathbf{r}}_{\perp}$ are unit vectors parallel and perpendicular to the local mean field \mathbf{B}_L , respectively. See Cho & Vishniac (2000) for the detailed discussion of the local frame. Left panel of Fig. 5 is an example of such visualization⁷. The horizontal axis corresponds to the local mean field directions. The shapes of contours illustrate scale-dependent anisotropy: the large eddies are roughly isotropic and smaller eddies are more elongated. However, we should be careful when we derive a quantitative scaling relation for anisotropy from the contour diagram.

The 2-point second-order structure function of a variable A

$$SF_2(r) = (\delta A_r)^2 = \langle |A(\mathbf{x} + \mathbf{r}) - A(\mathbf{x})|^2 \rangle \quad (36)$$

is in general related to the energy spectrum of the variable, $E_A(k)$, through

$$SF_2(r) = (\delta A_r)^2 \sim k E_A(k), \quad (37)$$

where $k \propto 1/r$ is the wavenumber. Therefore, when $E_A(k) \propto k^{-m}$, we have

$$SF_2(r) \propto r^{m-1}. \quad (38)$$

For example, in fully developed Kolmogorov turbulence ($E(k) \propto k^{-5/3}$), the scaling relation of the second-order longitudinal structure function is given by

$$SF_2(r) = (\delta v_r)^2 \sim k k^{-5/3} \propto k^{-2/3} \propto r^{2/3}. \quad (39)$$

However, when the slope of the turbulence spectrum is steeper than k^{-3} , the relation in Eq. (37) becomes invalid

⁶ We use a similar filtering method as in the previous subsection. We obtain the local mean field, \mathbf{B}_L , by eliminating Fourier modes whose perpendicular wavenumber is greater than $k/2$. We obtain the fluctuating field, \mathbf{b}_l , by eliminating Fourier modes whose perpendicular wavenumber is less than $k/2$ or greater than $2k$. Note that $l = 2\pi/k$, or in terms of grid units $l = N_{side}/k$, where $N_{side} = 512$ in Run E512D.

⁷ Note however that we do not use the usual 2-point second-order structure function for the plot. Instead, we use the 5-point second-order structure function that will be discussed later in this subsection.

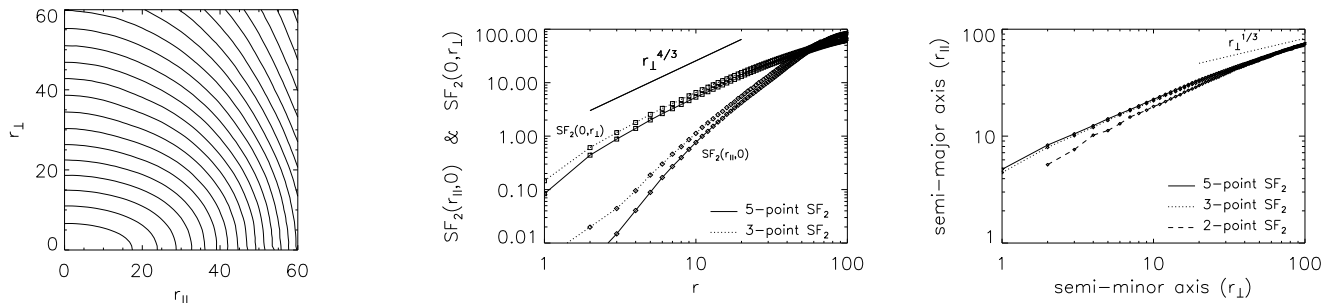


FIG. 5.— Anisotropy from the second-order structure function (Run E512D). *Left*: contour diagram obtained from the 5-point second-order structure function. *Middle*: comparison of the 3-point SF_2 and the 5-point SF_2 . The parallel structure function $SF_2(r_{\parallel}, 0)$, for example, can be obtained from values of SF_2 on the horizontal axis of the contour diagram. *Right*: the relation between the semi-minor axis ($\propto 1/k_{\perp}$) and the semi-major axis ($\propto 1/k_{\parallel}$) of the contours.

and $SF_2(r) \propto r^2$ regardless of the slope of the energy spectrum (see Appendix B). In EMHD, the energy spectrum expressed in terms of k_{\perp} scales as $E(k_{\perp}) \propto k_{\perp}^{-7/3}$ and we expect that the second-order structure function scales as

$$SF_2(0, r_{\perp}) \propto r_{\perp}^{4/3}. \quad (40)$$

On the other hand, the energy spectrum expressed in terms of k_{\parallel} is expected to be $E(k_{\parallel}) \propto k_{\parallel}^{-5}$ when anisotropy scales as $k_{\parallel} \propto k_{\perp}^{1/3}$ (see CL04). Therefore, the one-to-one correspondence between the second-order structure function and the energy spectrum is not valid for parallel direction. This means we cannot use the second-order structure function to reveal true anisotropy.

We have shown that the 2-point second-order structure function is not suitable for quantitative study of anisotropy in EMHD turbulence. However, it is possible to construct multi-point second-order structure functions that can be used for variables with steep energy spectra (see Falcon, Fauve, & Laroche 2007; Lazarian & Pogoyan 2008; see also Appendix C). The 3-point SF_2 was used by Falcon et al. (2007) and Lazarian & Pogoyan (2008). The 3-point SF_2 will work for energy spectrum as steep as $\sim k^{-5}$. In Appendix C, we discuss how to construct 4-point and 5-point structure functions. The 5-point SF_2 works for energy spectrum as steep as $\sim k^{-9}$.

Left panel of Fig. 5 is obtained with this 5-point structure function. Middle panel of the Figure shows the parallel structure functions, $SF_2(r_{\parallel}, 0)$, and the perpendicular structure functions, $SF_2(0, r_{\perp})$. We plot the results of 3-point (dotted lines) and 5-point (solid lines) structure functions. In the perpendicular direction, both structure functions reasonably follow the expected scaling of $r_{\perp}^{4/3}$. In the parallel directions, however, we observe that, when $r_{\parallel} \gtrsim 10$, the structure functions are much shallower than the expected scaling of r_{\parallel}^4 , which is from $SF_2 \propto k_{\parallel} E(k_{\parallel}) \propto k_{\parallel}^{-4} \propto r_{\parallel}^4$. In the parallel directions, the 5-point structure function is steeper than the 3-point one.

One should note that it is very difficult to obtain a well-defined power-law scaling for the parallel direction. This is because the inertial range in the parallel direction, if any, is extremely short. In the perpendicular direction, the inertial range spans from the outer scale ($k_{\perp} \sim 3$) to the dissipation scale ($k_{\perp} \sim 100$). Suppose that $k_{\parallel} \propto k_{\perp}^{1/3}$ is the true anisotropy. Then, in the parallel direction, the inertial range spans from $k_{\parallel} \sim 3$ to $k_{\parallel} \sim 3 \times (100/3)^{1/3} \sim 10$.

Therefore, it is virtually hopeless to reveal true anisotropy from contour diagram. Indeed, right panel of Fig. 5 shows that the anisotropy derived from the relation between semi-major axis and semi-minor axis of contours is not really consistent with the $k_{\parallel} \propto k_{\perp}^{1/3}$ relation. Both the solid curve (5-point) and the dotted curve (3-point) show a similar scaling. The average slope is approximately ~ 0.5 . Therefore, we can conclude that true anisotropy is similar to or stronger than this. Note that the dashed curve (2-point) show a milder anisotropy (or, a steeper slope). This means that multi-point structure functions are indeed better for steep spectrum. Although structure functions may not be suitable to reveal true anisotropy for EMHD, it is promising that multi-point structure functions seem to resolve steeper spectrum better.

6.4. Decaying vs. Forced EMHD turbulence

It is generally true that both decaying and driven turbulence show a similar scaling. However, in the presence of strong mean magnetic field, it is not clear whether or not they really show a similar scaling. Consider a decaying strongly magnetized EMHD turbulence. Let us assume that critical balance is roughly satisfied at $t=0$. The strength of random magnetic field drops as time goes on. But, the strength of the mean magnetic field remains same. Therefore, critical balance will be soon destroyed. Of course, there is a narrow window of time during which critical balance is satisfied and we can study critically balanced EMHD turbulence during the time interval. Nevertheless, it is worth comparing driven turbulence and decaying turbulence. In this section, we show that forced EMHD turbulence exhibits similar scaling relations as decaying EMHD turbulence.

Numerical setup for driven EMHD turbulence is similar to that of decaying EMHD turbulence. Forcing is done in Fourier space. The forcing term consists of 21 Fourier components with $2 \leq k \leq \sqrt{12}$. The peak of energy injection is at $k \approx 2.5$. The forcing is statistically isotropic. The strength of the mean magnetic field B_0 is 1. We adjusted the amplitudes of the forcing components so that $b \approx 1$. Therefore, the driven EMHD turbulence satisfies the condition for critical balance. This run is designated as Run E256F in Table 1.

Inset in Fig. 6 shows time evolution of magnetic energy density (in fact $B^2 = B_0^2 + b^2$). The magnetic energy

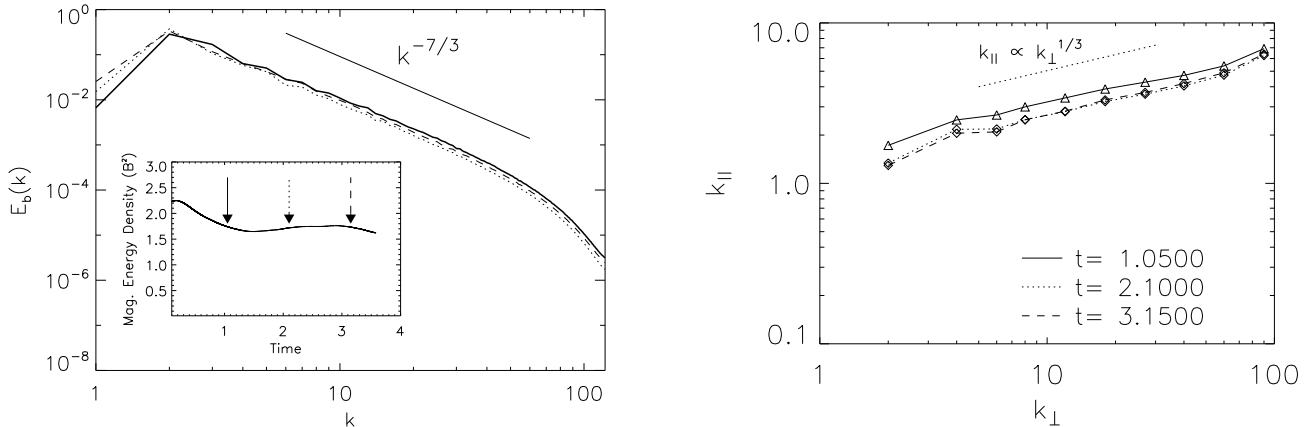


FIG. 6.— Driven EMHD turbulence (Run E256F). The strength of the (global) mean field is 1 (i.e. $B_0 = 1$). The strength of the fluctuating magnetic field (b) is maintained to be ~ 1 . Since driving is isotropic, the critical balance is satisfied. *Left*: time evolution of magnetic energy density (inset) and energy spectra. The spectra are taken at 3 different time points marked by the arrows in the inset. *Right*: anisotropy. Line styles of the curves are the same as those of the arrows in the inset.

reaches a stationary state after $t \sim 1$. The main plot of Fig. 6 shows magnetic energy spectrum at 3 different time points marked by the arrows in the inset. Line styles of the spectra are the same as those of the arrows. The slopes of all 3 energy spectra are consistent with $-7/3$.

We plot anisotropy in right panel of Fig. 6. We use the technique described in Section §6.1. Anisotropy of driven EMHD turbulence is also consistent with the $k_{||} \propto k_{\perp}^{1/3}$ scaling. All in all, driven MHD turbulence shows similar spectrum and anisotropy as decaying EMHD turbulence.

6.5. Inverse cascade of EMHD turbulence

In Wareing & Hollerbach (2009) the inverse cascade was reported as a part of decaying 2D EMHD turbulence. The energy spectrum in Shaikh & Zank (2005) also shows a clear evidence of inverse cascade in driven 2D EMHD turbulence. However, the difference of 3D and 2D turbulence makes one wonder whether the inverse cascade is present in decaying 3D EMHD turbulence.

We perform another decaying EMHD turbulence simulation. The numerical setup is almost identical to the one described in Section §4.1. However, we use a different initial condition. At $t = 0$, Fourier modes with $16 \leq k \leq 32$ are excited (see the solid curve in Left panel of Fig. 7). The numerical resolution is 256^3 . This run is not listed in Table 1.

Left panel of Fig. 7 shows spectral behavior of the decaying EMHD turbulence. The dotted line shows the spectrum shortly after the simulation. The dotted line clearly shows that most of the energy cascades down to small scales. Of course, the energy cascading down to small scales will dissipate away below $k \gtrsim 80$. It also shows that some of the energy goes to larger scales, the amount of which is smaller than that in the 2D EMHD case (see Wareing & Hollerbach 2009). At later times, the peak to the energy spectrum moves to larger scales, which probably means that we see a self-similar decaying of energy that leads to the increase of the integral scale (see, for example, Biskamp 2003), rather than a signature of the inverse energy cascade that is observed in 2D hydrody-

namic turbulence. Nevertheless, we clearly observe that EMHD turbulence can generate more coherent magnetic field from a smaller scale, hence less coherent, magnetic field. Although this phenomenon is not the inverse cascade per se, we can still call it inverse cascade because it does show that small amount of energy goes to larger scales. However, in order to avoid confusions, we will use the term ‘small amount of inverse cascade’ whenever possible.

We compare our results with the spectral behavior of the decaying 3D MHD turbulence in Right panel of Fig. 7. At $t = 0$ velocity field has a flat spectrum between $k = 16$ and $k = 32$ (solid curve). The magnetic field at $t = 0$ has only the uniform component, the strength of which is set to 1. The numerical resolution is also 256^3 and this run is not listed in Table 1. At later times, the velocity field generates fluctuating magnetic field mainly between $k = 16$ and $k = 32$. We see that MHD turbulence also shows small amount of inverse cascade. Overall spectral behavior of decaying MHD turbulence is similar to that of decaying EMHD turbulence. However, there are also differences. For example, the gradual shift of the peak of the energy spectrum to larger scale is less pronounced in the MHD case. The slopes of the energy spectra on large scales are also different.

7. HIGH-ORDER STATISTICS AND BISPECTRUM OF EMHD

In this section, we present other statistical properties of EMHD turbulence. We use a data cube from Run E512D, which is the the same data cube as we considered in Section §6.

7.1. High-order structure functions

High-order structure functions are used for the study of intermittency, which refers to the non-uniform distribution of structures. The structure functions of order p for magnetic field is defined by

$$SF_p(r) = \langle |\mathbf{B}(\mathbf{x}) - \mathbf{B}(\mathbf{x} + \mathbf{r})|^p \rangle_{avg. over x}. \quad (41)$$

Traditionally, researchers use high-order structure functions of velocity to probe dissipation structures of turbulence. In fully developed hydrodynamic turbulence,

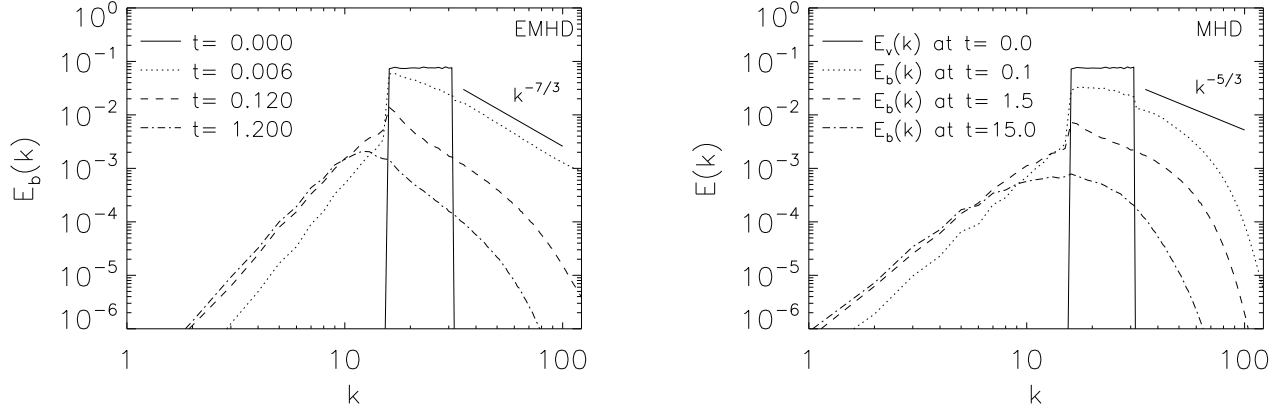


FIG. 7.— Spectra of decaying turbulence. The mean field (B_0) is set to 1 in both cases. *Left*: EMHD turbulence. At $t = 0$, the magnetic spectrum is flat for $16 \leq k \leq 32$ (solid curve). At later times, energy cascades down to smaller scales. At the same time, some energy cascades inversely up to larger scales. *Right*: MHD turbulence. At $t = 0$, the *velocity* spectrum is flat for $16 \leq k \leq 32$ (solid curve). The magnetic field has only the uniform component (B_0) at $t = 0$. At later times, random magnetic field is generated and most of the turbulence energy cascades down to smaller scales. We also observe inverse cascade. Note that, in the right panel, the solid line is for velocity at $t=0$ and other lines are for magnetic field at later times.

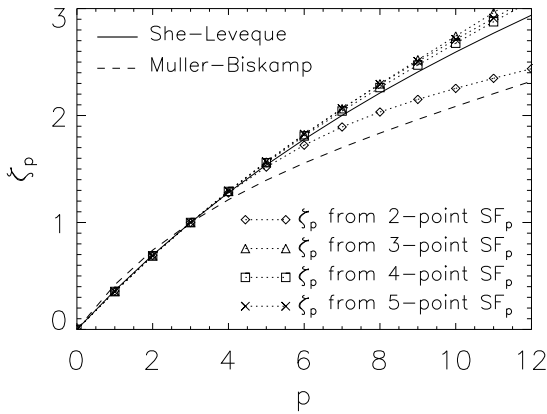


FIG. 8.— Intermittency (Run E512D). Scaling exponents from the 3-point, the 4-point, and the 5-point structure functions follow the She-Leveque scaling. However, those from the standard 2-point structure function show a different scaling. The ζ_p 's shown here are the relative scaling exponents, ζ_p/ζ_3 .

the (longitudinal) velocity structure functions $SF_p = \langle ([\mathbf{v}(\mathbf{x} + \mathbf{r}) - \mathbf{v}(\mathbf{x})] \cdot \hat{\mathbf{r}})^p \rangle \equiv \langle (\delta v_r)^p \rangle$ are expected to scale as r^{ζ_p} . One of the key issues in this field is the functional form of the scaling exponents ζ_p . There are several models for ζ_p . Roughly speaking, the dimensionality of the dissipation structures plays an important role.

Assuming 1-dimensional worm-like dissipation structures, She & Leveque (1994) proposed the scaling relation

$$\zeta_p^{SL} = p/9 + 2[1 - (2/3)^{p/3}] \quad (42)$$

for incompressible hydrodynamic turbulence. On the other hand, assuming 2-dimensional sheet-like dissipation structures, Müller & Biskamp (2000) proposed the relation

$$\zeta_p^{MB} = p/9 + 1 - (1/3)^{p/3} \quad (43)$$

for incompressible magneto-hydrodynamic turbulence. There are other models for intermittency. But, in this paper, we only consider above mentioned two models because they are relevant to incompressible variables.

In this paper, we only consider structure functions in perpendicular directions. That is, in our calculations, the vector \mathbf{r} (see Eq. [41]) is perpendicular to the direction of the local mean field, \mathbf{B}_L . The reason why we do not consider parallel direction is that structure functions are not suitable for revealing true scaling relation in parallel directions. In Fig. 8 we plot the relative scaling exponent ζ_p/ζ_3 for EMHD turbulence⁸. It is interesting that the 2-point structure functions show a different scaling exponents com-

⁸ In hydrodynamic turbulence, the relative scaling exponents are expressed relative to ζ_3 since Kolmogorov's four-fifth law is valid for the third-order longitudinal structure function: $SF_3 \propto r$, where the constant of proportionality is $(-4/5)$ times the energy injection rate. Therefore, it is natural to use ζ_3 for the relative scaling exponents. In MHD, there also exists a similar exact relation for a third-order structure function expressed in terms of Elsasser variables (Politano & Pouquet 1998). However, according to the exact correlation law obtained by Galtier (2008), there is no simple relation between SF_3 and r in EMHD and, therefore, the use of ζ_3 for the relative scaling exponents is not justified. Nevertheless, for the sake of comparison with existing models, we use ζ_3 for the Figure.

pared with other multi-point structure functions. This result is not surprising because we already observed that the 2-point second-order structure function shows a different behavior compared with other multi-point structure functions in right panel of Fig. 5. The scaling exponents based on the 3-point, the 4-point, and the 5-point structure functions are consistent with the She-Leveque model.

7.2. Bispectrum

In astronomy, the bispectrum is a tool widely used in cosmology and gravitational wave studies (Fry 1998; Scocimarro 2000; Liguori et al. 2006). Here, we briefly describe the definition of the bispectrum (see Burkhart et al. 2009). The bispectrum is closely related to the power spectrum. The Fourier transform of the second-order cumulant, i.e. the autocorrelation function, is the power spectrum while the Fourier transform of the third order cumulant is known as the bispectrum. In a discrete system, the bispectrum is defined as:

$$BS(\vec{k}_1, \vec{k}_2) = \sum_{\vec{k}_1=const} \sum_{\vec{k}_2=const} \tilde{A}(\vec{k}_1) \cdot \tilde{A}(\vec{k}_2) \cdot \tilde{A}^*(\vec{k}_1 + \vec{k}_2) \quad (44)$$

where k_1 and k_2 are the wave numbers of two interacting waves, and $A(\vec{k})$ is the original discrete data with finite number of elements with $A^*(\vec{k})$ representing the complex conjugate of $A(\vec{k})$. As is shown in Equation (44), the bispectrum is a complex quantity which will measure both phase and magnitude information between different wave modes.

Original formalism for bispectrum is suitable for scalar variables. Since we deal with magnetic field, which is a vector quantity, we simply take z-component of magnetic field. Note that $\mathbf{B}_0 = B_0 \hat{\mathbf{z}}$. In Fig. 9, we plot bispectrum of driven EMHD (left panel), decaying EMHD (middle panel), and driven MHD (right panel). For the driven EMHD and MHD turbulence cases, we take the data after turbulence has reached statistically stationary state ($t \sim 3$ and $t \sim 45$, respectively). The decaying EMHD case was taken at $t \sim 3$ (see the inset of Fig. 1). Both driven EMHD (left panel) and decaying EMHD (middle panel) cases show similar bispectrum. However, driven MHD (right panel) shows a substantially different bispectrum. All cases show that amplitudes of bispectra are highest when $k_1 = k_2$, which means a high correlation of modes at $k_1 = k_2$. The amplitudes of bispectra, hence strengths of nonlinear interactions, drop as we move away from the diagonal lines (i.e. the lines of $k_1 = k_2$). The shape of isocontours depends on the nature of nonlinear interactions. The case of the standard MHD (right panel) shows wider isocontours than EMHD cases, which means nonlinear interactions in standard MHD turbulence drop more slowly as we move away from the $k_1 = k_2$ line. This demonstrates that nonlinear interactions in EMHD and MHD cases are very different.

8. COMPARISON WITH THE SOLAR WIND TURBULENCE

In this subsection, we compare statistics of MHD/EMHD turbulence and turbulence in the solar wind. We consider quantities related to the probability distribution functions (PDFs) of fluctuations in increments of the

magnetic field strength B

$$dB \equiv \langle B(\mathbf{x} + \mathbf{r}) - B(\mathbf{x}) \rangle_x / \langle B(\mathbf{x}) \rangle_x, \quad (45)$$

where $B = |\mathbf{B}|$ is the strength of magnetic field and the angled brackets $\langle \dots \rangle_x$ denote average taken over \mathbf{x} . In this section, we are only concerned with characteristics of turbulence directly measured in space plasmas.

8.1. PDFs for dB

In the solar wind, the PDFs for increments of the magnetic field strength, dB , is measured by

$$dB(\tau) \equiv \langle B(t + \tau) - B(t) \rangle_t / \langle B(t) \rangle_t, \quad (46)$$

where $B(t)$ is the strength (or the averaged strength) of magnetic field at time t and $\langle \dots \rangle_t$ denotes average taken over time. The observed PDFs for dB on scales from 1 hour to 128 days are well described by the Tsallis distribution (Burlaga, F-Vinas, & Wang 2007; Burlaga & F-Vinas 2005), which is given by

$$y(x) = A \left[1 + (q-1) \frac{x^2}{w^2} \right]^{-1/(q-1)}, \quad (47)$$

where A , q , and w are constants. The function is proportional to a Gaussian function for small x ,

$$y(x) \approx A \left(1 - \frac{x^2}{w^2} \right) \approx A \exp\left(-\frac{x^2}{w^2}\right), \quad \text{as } x \rightarrow 0, \quad (48)$$

and a power law for large x ,

$$y(x) \propto x^{-2/(q-1)}, \quad \text{as } x \rightarrow \infty. \quad (49)$$

The shape of the function is determined by the values of q and w . In the limit of $q \rightarrow 1$, the function reduces to a Gaussian distribution. Therefore the value of q is a measure of non-Gaussianity. The value of w is related to the width of the distribution. Since $\tau > 1$ hour, the measured PDFs in Burlaga et al. (2007) and Burlaga & F-Vinas (2005) reflect fluctuations of MHD turbulence.

Fig. 10 shows PDFs of MHD (top panel) and EMHD (middle and bottom panels) turbulence. The solid lines are PDFs of dB in our numerical data and the dotted curves are fits of the PDFs to the Tsallis distribution. We use the Levenberg-Marquardt algorithm (Levenberg 1944; Marquardt 1963; see Press et al. 1992) for fitting. Each curve in the panels represents the PDF for a particular separation. As we move from the lowest curve in each panel, the separations in grid units are 2, 6, 10, 17, 29, 50, 88, respectively. Each curve is displaced vertically from the one below by a factor of 10. We set the value of each PDF at $dB = 0$ to 1 before displacement, for the sake of clarity.

The PDFs may depend on the direction of \mathbf{r} in Eq. (45). That is, the PDFs for the parallel direction can be different from those for perpendicular direction. Therefore, we calculate PDFs for parallel and perpendicular directions separately. We try both global and local frames to define parallel and perpendicular directions. Overall, we consider 4 cases: parallel direction in global frame ($r \parallel B_0$), parallel direction in local frame ($r \parallel B_L$), perpendicular direction in global frame ($r \perp B_0$), and perpendicular direction in local frame ($r \perp B_L$).

Our calculations show that there is no big difference in the PDFs of the above mentioned 4 cases. General trend is that the PDF is close to a Gaussian function when separation is large (upper curves in each panel) and it deviates from a Gaussian function when the separation is small (lower curves in each panel). We note however that, for a

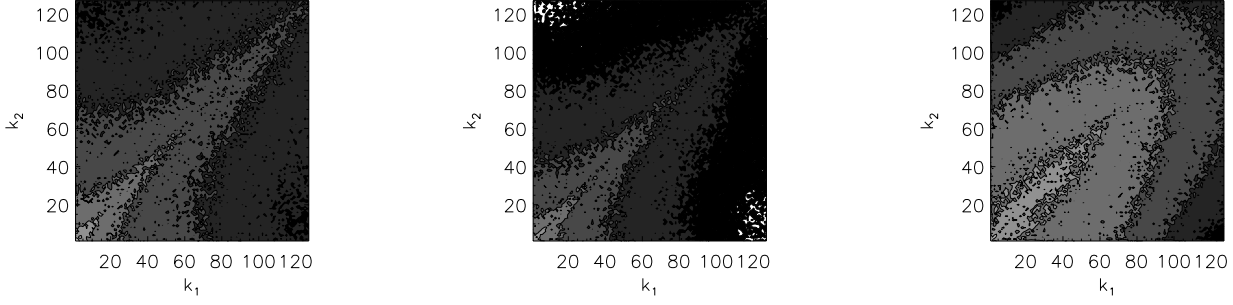


FIG. 9.— Bispectrum of EMHD (left and middle panels) and standard MHD (right panel). Driven EMHD turbulence at $t \sim 3$ (left panel; Run E256F) and decaying EMHD turbulence at $t \sim 3$ (middle panel; Run E256D) have similar bispectra. However, driven MHD turbulence at $t \sim 45$ (right panel; Run MHD256F) shows a different bispectrum.

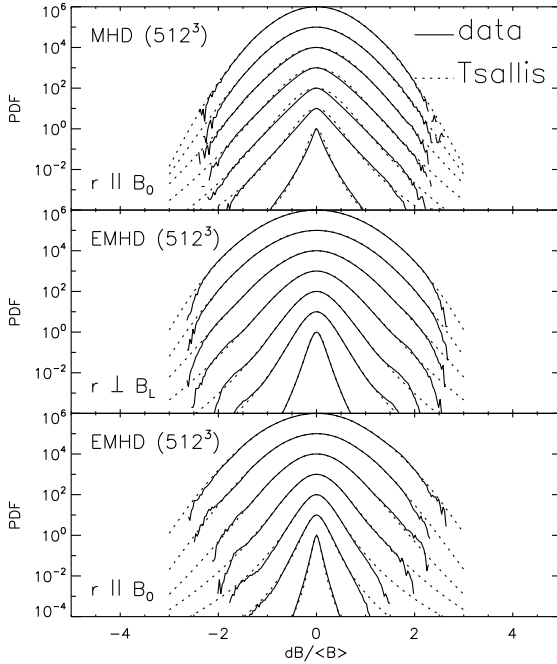


FIG. 10.— The PDFs for increments of magnetic field and Tsallis fit. The Tsallis distribution fits the PDFs well. The PDF is close to a Gaussian distribution when separation r is large (upper curves in each panel) and it deviates from a Gaussian function as the separation gets smaller (lower curves). Runs E512D (middle and lower panels) and MHD512F (upper panel) are used. Note that B_0 denotes the global mean field and B_L the local mean field. In each panel, curves correspond to $r = 2$ (lowermost curve), 6, 10, 17, 29, 50, 88 (uppermost curve), respectively.

given separation (for example, see the lowest curve in each panel, which corresponds to $r = 2$ grid units), the widths of the PDFs vary, depending on the direction of \mathbf{r} .

We can confirm quantitatively the trend that the PDF is close to a Gaussian distribution when separation is large and it deviates from a Gaussian distribution when the separation is small. In Fig. 11, we plot the values of q . The left panel is for EMHD turbulence (Run E512D) and the right panel for MHD turbulence (Run MHD512F). As we mentioned, the value of q is close to 1 when the PDF is close to a Gaussian distribution. Indeed, when the separation is large, q is very close to 1. The value of q deviates from 1 as the separation gets smaller, which means that the PDF deviates from a Gaussian distribution. The overall trend is consistent with the observations of the MHD-scale fluctuations in the solar wind (see Burlaga & F-Vinas 2005; Burlaga et al. 2007). But, this should be taken as a very

approximate statement, because the behavior of q in the solar wind is very complicated. In each panel of Fig. 11, we plot the q values of 4 different directions mentioned above. In general, all 4 cases show a similar trend, although the q values for the parallel cases are slightly larger than those for perpendicular cases.

In Fig. 12, we plot the values of w . The left panel is for EMHD turbulence (Run E512D) and the right panel for MHD turbulence (Run MHD512F). It is interesting that the values of w in EMHD cases show steeper dependence on separation than those of MHD cases. One should also note that the behavior of q as well as w for parallel directions in EMHD cases may be dominated by large-scale fluctuations, because the energy spectrum $E(k_{\parallel})$ is too steep (see Section §6.3 and Appendix B).

Fig. 12 shows that the values of w for perpendicular direction (dotted lines) are systematically larger than those

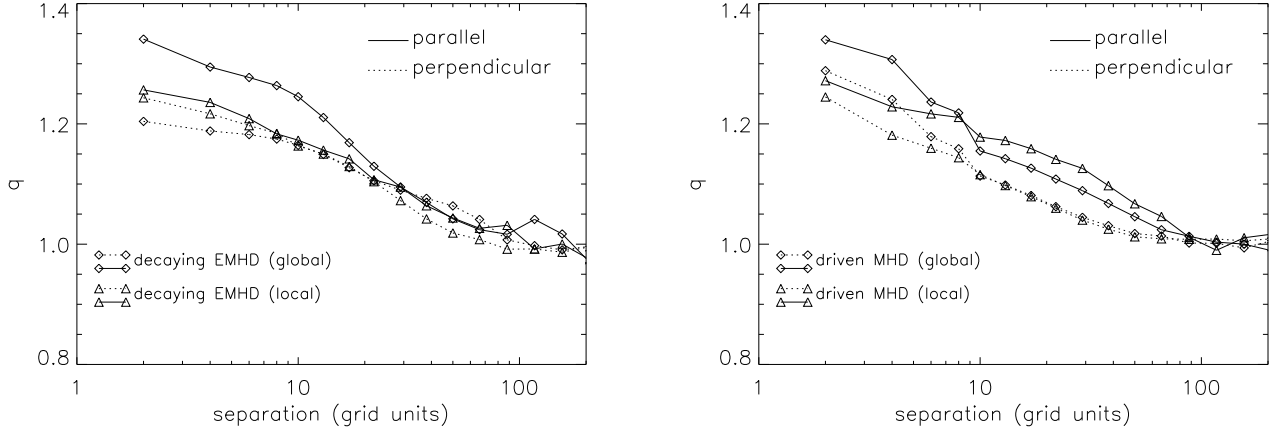


FIG. 11.— The q parameter of Tsallis distribution. When the separation is large the values of q are very close to 1, while they are larger for smaller separations. Note that $q = 1$ corresponds to a Gaussian distribution. Runs E512D (left panel) and MHD512F (right panel) are used.

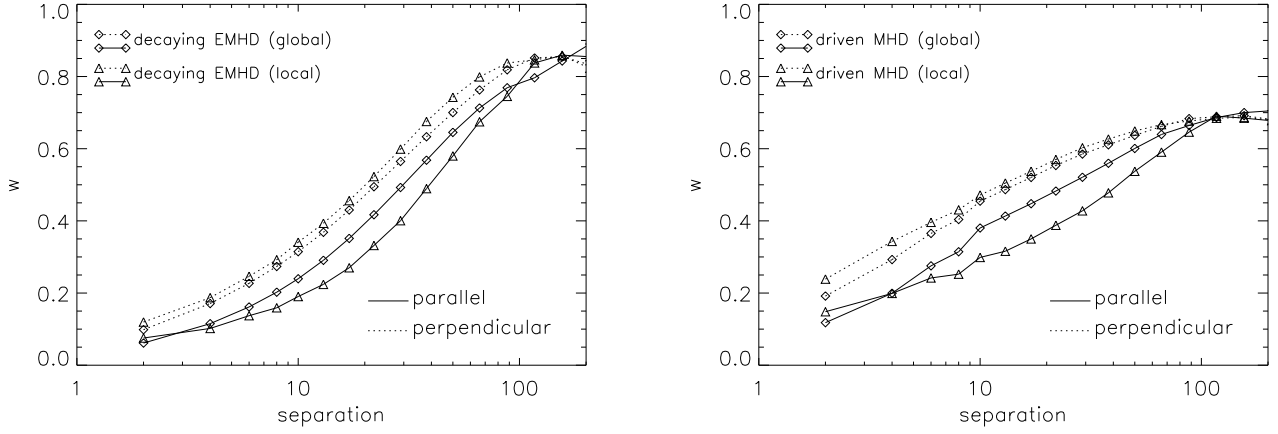


FIG. 12.— The w parameter of Tsallis distribution. When the separation is larger the values of w is larger. The EMHD case (left panel) shows a stronger dependence on the separation. Runs E512D (left panel) and MHD512F (right panel) are used.

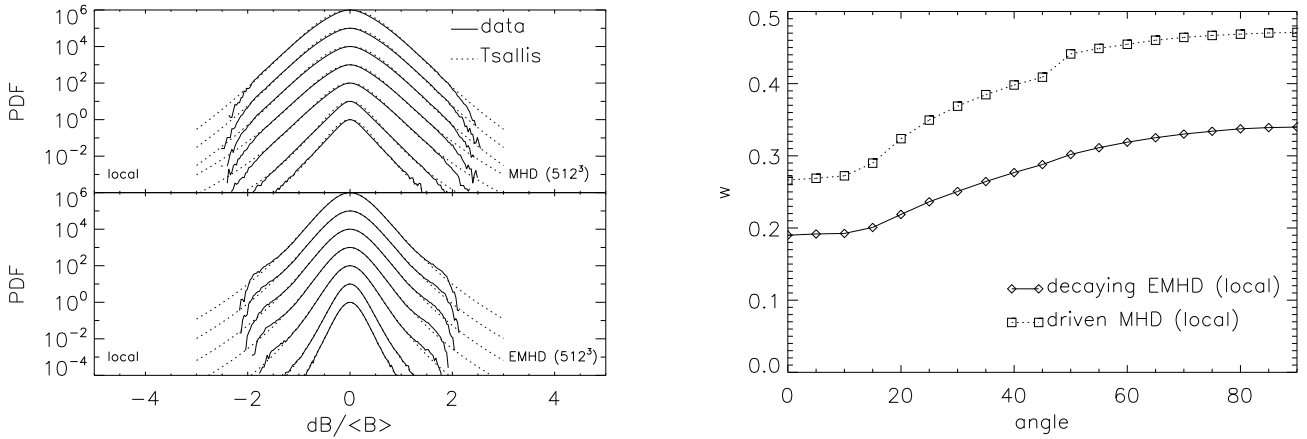


FIG. 13.— Angular dependence of the w parameter of Tsallis distribution. *Left*: The PDFs for dB and Tsallis fit. The curves in each panel correspond to $\theta = 0^\circ$ (lowermost curve), 15° , 30° , 45° , 60° , 75° , and 90° (uppermost curve), respectively. θ is the angle between *local* mean magnetic field and the direction of \mathbf{r} . *Right*: Dependence of w on θ . The horizontal axis is θ in degrees. Runs E512D (EMHD) and MHD512F (MHD) are used. All calculations are done in local frame.

for parallel direction (solid lines). Fig. 13 shows that w parameter indeed depends on the direction of \mathbf{r} . The

curves in the left panel are the PDFs for different values of θ , which is the angle between the *local* mean magnetic field and the separation vector \mathbf{r} . The curves in top or bottom panel correspond to $\theta = 0^\circ$ (lowermost curve), $15^\circ, 30^\circ, 45^\circ, 60^\circ, 75^\circ$, and 90° (uppermost curve), respectively. We can clearly see that the width of the PDF gets larger as the angle increases. Note that the w parameter of Tsallis distribution is related to the width of the PDF. The right panel quantitatively shows dependence of w on θ . The w parameter is smallest when $\theta = 0$ (=parallel direction) and it is largest when $\theta = 90^\circ$ (perpendicular direction).

8.2. PDFs for wavelet transform coefficients

The wavelet transform is sometimes used for the study of the magnetic field fluctuation in the solar wind. For example, Alexandrova et al. (2008) used the Morlet wavelet transform

$$\mathcal{W}_i(\tau, t) = \sum_{j=0}^{N-1} B_i(t_j) \psi[(t_j - t)/\tau], \quad (50)$$

where $B_i(t_j)$ is the i th component of the magnetic field at $t_j = t_0 + j \times \Delta t$, and $\psi(u) \propto \cos(6u) \exp(-u^2/2)$ is the Morlet wavelet. In this subsection, we briefly consider PDFs of the Morlet wavelet transform coefficient \mathcal{W}_i .

We perform the Morlet wavelet transform using our numerical data. We only consider the parallel (or z) component of magnetic field in global frame. Note that, in our numerical calculations, τ in Eq. (50) is proportional to separation r and the global mean magnetic field \mathbf{B}_0 is parallel to z -direction. Fig. 14 shows that the Tsallis distributions roughly fit the PDFs of EMHD turbulence (Run E512D).

The horizontal axis is $\mathcal{W}_z(\tau)/\langle \mathcal{W}_z(\tau)^2 \rangle_t^{1/2}$. In general the PDFs for large separations (upper curves in each panel) are close to Gaussian distributions and those for small separations (lower curves in each panel) show departure from Gaussian ones. The PDFs for the parallel direction (lower panel) show stronger departure from Gaussian distributions, which is confirmed by the large values of q for small separations (not shown in this paper). In the right panel of the Figure, we show the flatness (or Kurtosis) as a function of the scale, which is defined by

$$\langle \mathcal{W}_i^4 \rangle / \langle \mathcal{W}_i^2 \rangle^2. \quad (51)$$

We show both MHD and EMHD cases in the same plot. In the case EMHD, we show the flatness of both dB_z and \mathcal{W}_z . In the case of MHD, we show the flatness of dB_z only. When the separation is large, the flatness is very close to the Gaussian value of 3. In general, it increases as the separation decreases, which is consistent with observations (Carbone et al. 2004; Alexandrova et al. 2008; see also Burlaga & F-Vinas 2005). Note that flatness of \mathcal{W}_z of EMHD turbulence in the parallel direction shows a strong dependence on the separation.

9. DISCUSSIONS

9.1. Anisotropy of EMHD

Anisotropy of EMHD is impossible to measure using the traditional second order structure function. In CL04, we

proposed to a different technique which allowed us to actually get $k_{\parallel} \sim k_{\perp}^{1/3}$, which confirmed our theoretical prediction.

However, as the problem of measuring anisotropy is important, in the present paper we provided not only higher resolution simulations, but also a few new techniques of measuring anisotropy. All these techniques provided results consistent with our earlier finding.

Unlike CL04, in this paper we did not limit ourselves by the simulations of the decaying turbulence, but also studied driven turbulence. We did not observe differences in the slope or spectrum between the two cases.

9.2. EMHD and Kinetic Alfvén wave turbulence

As we have shown in §2, there are two approaches to describing the turbulence over scales less than the proton gyroscale. The traditional approach assumes that the term proportional to $\nabla \cdot \mathbf{v}$ (see Eq. [14]) is negligible, while the approach in Schekochihin et al. (2009) insists on keeping this term. We performed numerical simulations with and without the term and obtained virtually identical results for the turbulence spectrum and anisotropy. This result shows importance of EMHD to analyze collisionless plasmas.

CL04 derived the anisotropy of the EMHD turbulence and confirmed the obtained scaling numerically. Recently, Howes et al. (2008a) used a gyrokinetic code and obtained the expected $k^{-7/3}$ energy spectrum for magnetic fluctuations below the proton gyroscale (see also discussions in Matthaeus et al. 2008 and Howes et al. 2008b). Anisotropy has not been studied with a gyrokinetic code yet.

9.3. MHD and EMHD turbulence

Within the paper we have employed a set of different statistical measures to characterize EMHD turbulence. We compared the results with those obtained for MHD turbulence. We found both similarities and differences between the two types of turbulence.

MHD turbulence and EMHD turbulence have different energy spectra and anisotropy in spite of the fact that their scaling relations are derived from the same principles: constancy of energy cascade and critical balance. Our confirmation of the anisotropy scaling predicted in CL04 testifies that the importance of the critical balance goes beyond MHD.

Surprisingly, the high-order statistics shows a similar scaling: scaling exponents of both MHD turbulence (see Cho, Lazarian & Vishniac 2002) and EMHD turbulence are compatible with those of the She-Leveque scaling⁹. Does it mean that the She-Leveque scaling is so universal that it fails to distinguish different types of turbulence? What is the underlying reason for this universality? These are still open questions to be addressed by the future research.

Interestingly enough, the PDFs for increments of magnetic field are well described by the Tsallis function. The correspondence between the space measurements and Tsallis description can be found, for example, in Burlaga & F.-Vinas (2005), Leubner & Vörös (2005), and Burlaga

⁹ Note however that we considered turbulence in strongly magnetized medium and that the SF_p we measured are for directions perpendicular to the local mean field \mathbf{B}_L .

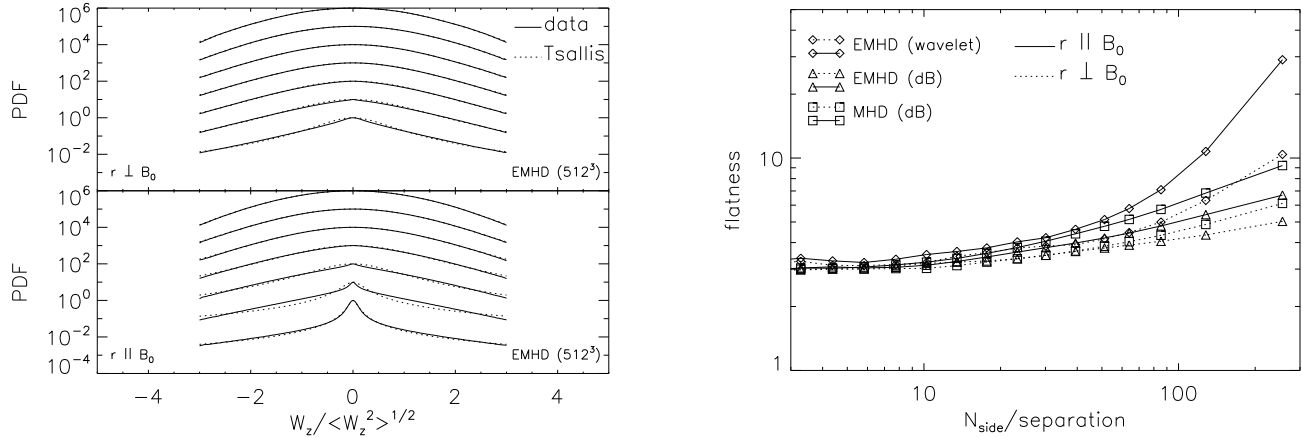


FIG. 14.— The PDF and flatness (Kurtosis) of the Morlet wavelet transformation coefficient W_z , where z is parallel to the global mean field \mathbf{B}_0 . *Left*: the Tsallis distribution approximately fits the PDFs. In each panel, curves correspond to $r = 2$ (lowermost curve), 6, 10, 17, 29, 50, 88 (uppermost curve), respectively. *Right*: flatness is larger for smaller separation. When the separations are large, the measured values of the flatness are very close to 3, which is the same as the flatness of the normal distribution.

et al. (2007). Now we confirmed the correspondence with direct numerical simulations.

Another statistics, namely, the bispectrum is very different for MHD and EMHD. The bispectrum measures non-linear interactions. The difference observed confirms the difference in cascading of the two types of turbulence.

9.4. Inverse cascade in EMHD

Our simulations in §6.5 show the existence of small amount of inverse cascade in decaying EMHD turbulence. Although we have not performed simulations with driven turbulence, we expect that small amount of inverse cascade is an intrinsic part of the EMHD cascade. That is, we expect that generation of small amount of larger scale, hence more coherent, magnetic field from small scale turbulence is an intrinsic part of the EMHD turbulence.

This kind of inverse cascade has important implications in the 3D MHD case. When there exists turbulent velocity cascade, this kind of inverse cascade enables generation of coherent field on the outer scale of turbulence from a small-scale seed magnetic field (see Cho et al. 2009). Note, however, that the existence of turbulent velocity cascade that can amplify the magnetic field is assumed here. In EMHD, on the contrary, the fluctuations of magnetic field and velocity are connected with each other from the very beginning. Nevertheless, one can speculate that the small amount of inverse cascade in EMHD turbulence can help to create large scale magnetic structures when the driving is at small scales. An interesting implication of this kind of inverse EMHD cascade could be its contribution to the creation of the dipole field, when magnetic field is generated by the thermomagnetic instability in the crust of a neutron star.

9.5. Comparison with observations

Space plasma measurements allow for a direct comparison with the results of turbulence simulations. This comparison is essential, as numerically turbulence can be studied only for relatively small Reynolds and Lundquist numbers. As a result, validation of the obtained scaling in

realistic astrophysical environments is absolutely essential (see an extended discussion of the issue in Lazarian et al. 2009).

It is encouraging that the spectra and the PDFs of the increments of magnetic field strength obtained numerically show correspondence with observations. We believe that more detailed comparisons are necessary.

9.6. EMHD turbulence anisotropy and the ADAF model

The issue of why accretion disks around black holes are not as luminous as one would expect is a burning question, addressing of which is required for explaining the low luminosity of black hole environments in the centers of galaxies. One of the ideas proposed was that of Advection Dominated Accretion Flows (ADAFs) (Narayan & Yi 1995; Narayan et al. 1998). According to this idea the low luminosity of the accreting material is due to the low rate of the transfer of energy of the turbulent accreting flow to electrons. It is postulated in the model that protons carry the lion's share of the flow energy and thus the emission is suppressed. Is it so?

Quataert & Gruzinov (1999) discussed transition from standard Alfvénic MHD turbulence to EMHD turbulence in advection dominated accretion flows. As Alfvénic turbulence reaches the proton gyroradius scale, some of the turbulence energy goes to protons through collisionless damping. The major heating mechanism for protons right above the proton gyroscale is the transit time damping (TTD) caused by non-zero parallel magnetic field fluctuations. Heating of protons is sensitive to $\beta_i \approx (v_i/v_A)^2$, where v_A is the Alfvén speed. When $\beta_i \gg 1$, more protons are available for efficient interaction with Alfvén waves. Therefore, most of the turbulence energy goes to protons before it reaches the proton gyroscale. However, when $\beta_i \sim 1$, heating of protons is marginal and most of the turbulence energy will cascade down further, crossing the proton gyroscale (see Quataert 1999; Quataert & Gruzinov 1999).

The Alfvén waves will be converted into EMHD waves (whistlers) below the proton gyroradius scale. When EMHD turbulence is anisotropic (i.e. $k_{\parallel} \ll k_{\perp}$), heating

of protons by EMHD turbulence will be marginal because “protons sample a rapidly varying electromagnetic field in the course of a Larmor orbit (Quataert & Gruzinov 1999).” In this paper, we confirmed that anisotropy of EMHD turbulence ($k_{\parallel} \propto k_{\perp}^{1/3}$) is strong. Therefore, in this case, the remaining energy (that is, the energy that has survived the collisionless damping before the proton gyroradius scale) cannot heat protons. Instead, it will heat electrons when it reaches the electron gyroradius scale. The bottom line is that the strong anisotropy of EMHD turbulence will make heating of protons by EMHD turbulence rather difficult in collisionless astrophysical plasmas with $\beta_i \lesssim 1$ (see Quataert & Gruzinov 1999).

9.7. Other implications

Other applications of the EMHD model include collisionless magnetic reconnection in laboratory and space plasmas (Bulanov, Pegoraro, & Sakharov 1992; Biskamp, Schwarz, & Drake 1995; Avinash et al. 1998). Turbulence on microscale may be a source of anomalous resistivity, which can stabilize X-point reconnection. How important this type of reconnection is is a subject of debates. For instance, a model of magnetic reconnection in Lazarian & Vishniac (1999) appeals to the magnetic field weak stochasticity, rather than microphysical plasma effects to explain fast reconnection. Simulations by Kowal et al. (2009) successfully tested the Lazarian & Vishniac (1999) model, which may mean that in many astrophysically important cases the reconnection is fast irrespectively of the plasma properties. The anomalous effects, however, may be important for the initiation of the reconnection when the original level of turbulence in the system is low. In addition, in a partially ionized gas where the field wandering, which is the key element of Lazarian & Vishniac (1999) model, is partially suppressed, the anomalous plasma effects can be important for reconnection (Lazarian, Vishniac & Cho 2004). Incidentally, in the latter paper it is predicted that MHD turbulence is not killed by neutral friction in the partially ionized gas, but it gets resurrected at the scales at which neutrals and ions decouple. The resurrected cascade involves only ions and electrons, not neutrals, and may proceed as electron MHD cascade below the proton gyroscale.

In addition, properties of EMHD turbulence are important for understanding of physics of neutron star crusts (Cumming et al. 2004; Harding & Lai 2004) and acceleration of particles in Solar flares (Liu, Petrosian, & Mason 2006). While in most cases we view the EMHD cascade as the continuation of the MHD cascade below the proton gyroradius, for the crust of a neutral star the EMHD turbulence can be present on much larger scales. The main

assumption of the EMHD is that one can ignore the motions of protons. This is definitely the case of the neutron star’s solid crust.

10. SUMMARY

We have found the following results.

1. Electron MHD (EMHD) and Electron Reduced MHD (ERMHD) show identical scaling relations (both spectra and anisotropies).
2. High resolution EMHD simulation confirms $k^{-7/3}$ spectrum obtained by earlier studies (Biskamp, Schwarz, & Drake 1996; Biskamp et al. 1999; Ng et al. 2003; CL04). The spectrum of electric field is consistent with $k^{-1/3}$ spectrum obtained by earlier studies (see Schekochihin et al. 2009; Howes et al. 2008a; Dmitruk & Matthaeus 2006).
3. Our detailed study of anisotropy using different techniques supports $k_{\parallel} \propto k_{\perp}^{1/3}$ the EMHD scaling obtained by CL04.
4. Decaying EMHD turbulence and driven EMHD turbulence show the same scaling.
5. When we use three or larger number of points to define the structure functions, the scaling exponents of high-order structure functions follow a scaling similar to that of incompressible hydrodynamic turbulence.
6. Bispectrum of ERMHD turbulence, reflecting the coupling of different scales in the cascade, looks very different from that of standard MHD one.
7. The probability distribution functions (PDFs) of the increment of the magnetic field strength in EMHD and MHD cases are well described by the Tsallis distribution. The general trend of the PDFs is consistent with observations of the solar wind.

We thank the anonymous referee for useful suggestions/comments. J.C.’s work was supported by the Korea Research Foundation grant funded by the Korean Government (KRF-2006-331-C00136) and by KICOS through the grant K20702020016-07E0200-01610 provided by MOST. A.L. acknowledges the support by the NSF grants ATM 0648699 and AST 0808118. Both authors are supported by the NSF Center for Magnetic Self-Organization in Laboratory and Astrophysical Plasmas.

REFERENCES

- Alexandrova, O., Carbone, V., Veltri, P., & Sorriso-Valvo, L. 2008, *ApJ*, 674, 1153
- Avinash, K., Bulanov, S. V., Esirkepov, T., Kaw, P., Pegoraro, F., Sazorov, P. S., & Sen, A. 1998, *Phys. Plasmas* 5, 2849
- Bale, S. D., Kellogg, P. J., Mozer, F. S., Horbury, T. S., & Reme, H. 2005, *Physical Review Letters*, 94, 215002
- Barnes, A. 1966, *Physics of Fluids*, 9, 1483
- Biskamp, D. 2003, *Magnetohydrodynamic Turbulence* (Cambridge, UK: Cambridge University Press)
- Biskamp, D., Schwarz, E., & Drake, J. F. 1995, *Phys. Rev. Lett.* 75, 3850
- Biskamp, D., Schwarz, E., & Drake, J. F. 1996, *Phys. Rev. Lett.*, 76, 1264
- Biskamp, D., Schwarz, E., & Celani, A. 1998, *Physical Review Letters*, 81, 4855
- Biskamp, D., Schwarz, E., Zeiler, A., Celani, A., & Drake, J. F. 1999, *Phys. Plasmas*, 6, 751
- Burlaga, L. F., & Viñas, A.-F. 2005, *Journal of Geophysical Research (Space Physics)*, 110, 7110
- Burlaga, L. F., F-Viñas, A., & Wang, C. 2007, *Journal of Geophysical Research (Space Physics)*, 112, 7206

- Bulanov, S. V., Pegoraro, F., & Sakharov, A. S. 1992, *Phys. Fluids B*, 4, 2499
- Burkhart, B., Falceta-Gonçalves, D., Kowal, G., & Lazarian, A. 2009, *ApJ*, 693, 250
- Carbone, V., Bruno, R., Sorriso-Valvo, L., & Lepreti, F. 2004, *Planet. Space Sci.*, 52, 953
- Cho, J., & Lazarian, A. 2002, *Physical Review Letters*, 88, 245001
- Cho, J., & Lazarian, A. 2003, *MNRAS*, 345, 325
- Cho, J., & Lazarian, A. 2004, *ApJ*, 615, L41 (CL04)
- Cho, J., Lazarian, A., & Vishniac, E. T. 2002, *ApJ*, 564, 291
- Cho, J. & Vishniac, E. 2000, *ApJ*, 539, 273
- Cho, J., Vishniac, E. T., Beresnyak, A., Lazarian, A., & Ryu, D. 2009, *ApJ*, 693, 1449
- Cumming, A., Arras, P., & Zweibel, E. 2004, *ApJ*, 609, 999
- Dastgeer, S., Das, A., Kaw, P., & Diamond, P. 2000, *Phys. Plasmas*, 7, 571
- Dastgeer, S. & Zank, G. P. 2003, *ApJ*, 599, 715
- Dmitruk, P., & Matthaeus, W. H. 2006, *Physics of Plasmas*, 13, 042307
- Falcon, E., Fauve, S., & Laroche, C. 2007, *Physical Review Letters*, 98, 154501
- Fry, J. N. 1998, *New York Academy Sciences Annals*, 848, 62
- Galtier, S. 2006, *J. Plasma Phys.*, 72, 721
- Galtier, S. 2008, *Phys. Rev. E*, 77, 015302
- Galtier, S. & Bhattacharjee, A. 2003, *Phys. Plasmas*, 10, 3065
- Gary, S. P., Saito, S., & Li, H. 2008, *Geophys. Res. Lett.*, 35, 2104
- Goldreich, P., & Reisenegger, A. 1992, *ApJ*, 395, 250
- Goldreich, P., & Sridhar, S. 1995, *ApJ*, 438, 763
- Harding, A. K., & Lai, D. 2006, *Reports on Progress in Physics*, 69, 2631
- Howes, G. G., Dorland, W., Cowley, S. C., Hammett, G. W., Quataert, E., Schekochihin, A. A., & Tatsuno, T. 2008a, *Physical Review Letters*, 100, 065004
- Howes, G. G., Cowley, S. C., Dorland, W., Hammett, G. W., Quataert, E., Schekochihin, A. A., & Tatsuno, T. 2008b, *Physical Review Letters*, 101, 149502
- Kingsep, A. S., Chukbar, K. V., & Yan'kov, V. V. 1990, in *Reviews of Plasma Physics*, Vol. 16 (Consultants Bureau, New York)
- Kowal, G., Lazarian, A., Vishniac, E. T., & Otmianowska-Mazur, K. 2009, *ApJ*, in press, arXiv:0903.2052
- Kulsrud, R., & Pearce, W. P. 1969, *ApJ*, 156, 445
- Lazarian, A., & Pogosyan, D. 2008, *ApJ*, 686, 350
- Lazarian, A., Beresnyak, A., Yan, H., Opher, M., & Liu, Y. 2009, *Space Science Reviews*, 143, 387
- Lazarian, A., & Vishniac, E. T. 1999, *ApJ*, 517, 700
- Lazarian, A., Vishniac, E. T., & Cho, J. 2004, *ApJ*, 603, 180
- Leamon, R. J., Smith, C. W., Ness, N. F., Matthaeus, W. H., & Wong, H. K. 1998, *J. Geophys. Res.*, 103, 4775
- Leamon, R. J., Smith, C. W., Ness, N. F., & Wong, H. K. 1999, *J. Geophys. Res.*, 104, 22331
- Leubner, M. P., Vörös, Z. 2005, *ApJ*, 618, 547
- Levenberg, K. 1944, *The Quarterly of Applied Mathematics*, 2, 164
- Liguori, M., Hansen, F. K., Komatsu, E., Matarrese, S., & Riotto, A. 2006, *Phys. Rev. D*, 73, 043505
- Lithwick, Y., & Goldreich, P. 2001, *ApJ*, 562, 279
- Liu, S., Petrosian, V., & Mason, G. M. 2006, *ApJ*, 636, 462
- Maron, J., & Goldreich, P. 2001, *ApJ*, 554, 1175
- Marquardt, D. 1963, *SIAM Journal on Applied Mathematics*, 11, 431
- Matthaeus, W. H., Servidio, S., & Dmitruk, P. 2008, *Physical Review Letters*, 101, 149501
- Müller, W.-C., & Biskamp, D. 2000, *Physical Review Letters*, 84, 475
- Narayan, R., & Yi, I. 1995, *ApJ*, 452, 710
- Narayan, R., Mahadevan, R., Grindlay, J. E., Popham, R. G., & Gammie, C. 1998, *ApJ*, 492, 554
- Ng, C. S., Bhattacharjee, A., Germaschewski, K., & Galtier, S. 2003, *Phys. Plasmas*, 10, 1954
- Press, W. H., Teukolsky, S. A., Vetterling, W. T., & Flannery, B. P. 1992, *Numerical Recipes in Fortran*, (2nd ed., Cambridge: University Press)
- Politano, H., & Pouquet, A. 1998, *Phys. Rev. E*, 57, 21
- Saito, S., Gary, S. P., Li, H., & Narita, Y. 2008, *Physics of Plasmas*, 15, 102305
- Schekochihin, A. A., Cowley, S. C., Dorland, W., Hammett, G. W., Howes, G. G., Quataert, E., & Tatsuno, T. 2009, *ApJS*, 182, 310
- She, Z.-S., & Leveque, E. 1994, *Physical Review Letters*, 72, 336
- Shebalin, J. V., Matthaeus, W. H., & Montgomery, D. 1983, *Journal of Plasma Physics*, 29, 525
- Shaikh, D., & Zank, G. P. 2005, *Physics of Plasmas*, 12, 122310
- Smith, C. W., Hamilton, K., Vasquez, B. J., & Leamon, R. J. 2006, *ApJ*, 645, L85
- Scoccimarro, R. 2000, *ApJ*, 544, 597
- Stawicki, O., Gary, S. P., & Li, H. 2001, *J. Geophys. Res.*, 106, 8273
- Quataert, E. 1999, *High Energy Processes in Accreting Black Holes*, 161, 404
- Quataert, E. & Gruzinov, A. 1999, *ApJ*, 520, 248
- Wareing, C. J., & Hollerbach, R. 2009, *Physics of Plasmas*, 16, 042307

APPENDIX

A. DERIVATION OF ERMHD EQUATIONS

Schekochihin et al. (2009) first derived ERMHD from kinetic RMHD equations. They also gave derivation of ERMHD equations from the generalized Ohm's law. Therefore the starting point of ERMHD may be also the generalized Ohm's law. Derivation of ERMHD is almost identical to the EMHD case.

Here we briefly summarize the derivation of the ERMHD equation from the generalized Ohm's law. Detailed derivation can be found in Appendix of Schekochihin et al. (2009). The magnetic induction equation reads

$$\frac{\partial \mathbf{B}}{\partial t} = \nabla \times (\mathbf{v}_e \times \mathbf{B}), \quad (\text{A1})$$

TABLE 1
RUNS

Run	Resolution	B_0	b at $t=0$	k_{\perp} at $t=0^{\dagger}$	k_{\parallel} at $t=0^{\dagger}$	Comments
E512D	512 ³	1	1.21	$2 \leq k < 5$	$2 \leq k < 5$	decaying
E256D	256 ³	1	1.21	$2 \leq k < 5$	$2 \leq k < 5$	decaying
E256F	256 ³	1	1.21	$k \sim 2.5$	$k \sim 2.5$	forced
E256D-EL	768×256 ²	1	0.071	$4.5/\sqrt{2} \leq k_{\perp} \leq 4.5\sqrt{2}$	$1/3 \leq k_{\parallel} \leq 1$	decaying
ER256D1-EL	768×256 ²	1	0.071	$4.5/\sqrt{2} \leq k_{\perp} \leq 4.5\sqrt{2}$	$1/3 \leq k_{\parallel} \leq 1$	decaying, $\sqrt{\alpha} = 1$
ER256D8-EL	768×256 ²	1	0.071 [†]	$4.5/\sqrt{2} \leq k_{\perp} \leq 4.5\sqrt{2}$	$1/3 \leq k_{\parallel} \leq 1$	decaying, $\sqrt{\alpha} = 1/8$
MHD512F	512 ³	0.8	0	$k \sim 2.5$	$k \sim 2.5$	forced
MHD256F	256 ³	1	0	$k \sim 2.5$	$k \sim 2.5$	forced

[†]In this case, the value of \bar{b} at $t=0$ is listed.

[†]In cases of driven turbulence, the average driving-scale wavenumber is listed.

where

$$\mathbf{v}_e = \mathbf{v}_i - \frac{\mathbf{j}}{en_e} = \mathbf{v}_i - \frac{c}{4\pi en_e} \nabla \times \mathbf{B} \quad (\text{A2})$$

(see Appendix C of Schekochihin et al. 2009). Here we ignored magnetic dissipation. Note that the usual EMHD equations are also based on these equations. Substituting Eq. (A2) into Eq. (A1), we get

$$\frac{\partial \mathbf{B}}{\partial t} = \nabla \times \left[\mathbf{v}_i \times \mathbf{B} - \frac{c}{4\pi en_e} (\nabla \times \mathbf{B}) \times \mathbf{B} \right], \quad (\text{A3})$$

$$= -\mathbf{B} \nabla \cdot \mathbf{v}_i - \frac{c}{4\pi en_e} \nabla \times [(\nabla \times \mathbf{B}) \times \mathbf{B}] - \frac{c}{4\pi e} \left(\nabla \frac{1}{n_e} \right) \times [(\nabla \times \mathbf{B}) \times \mathbf{B}], \quad (\text{A4})$$

$$\approx -\mathbf{B} \nabla \cdot \mathbf{v}_i - \frac{c}{4\pi en_e} \nabla \times [(\nabla \times \mathbf{B}) \times \mathbf{B}], \quad (\text{A5})$$

$$= -\mathbf{B} \nabla \cdot \mathbf{v}_i - \frac{c}{4\pi en_e} \nabla \times [\mathbf{B} \cdot \nabla \mathbf{B}], \quad (\text{A6})$$

which is the same as the EMHD equation except the $\mathbf{B} \nabla \cdot \mathbf{v}_i$ term on the right. Here we assume $\mathbf{v}_i \approx 0$, but $\nabla \cdot \mathbf{v}_i = \nabla \cdot \mathbf{v}_e \neq 0$. We ignore the last term of Eq. (A4) because it is $\sim O(\epsilon^2)$. According to the RMHD ordering (see Section 2 of Schekochihin et al. 2009), we have

$$\frac{\delta n_e}{n_e} \sim \frac{b}{B_0} \sim \frac{k_{\parallel}}{k_{\perp}} = \epsilon \ll 1, \quad (\text{A7})$$

where δn_e is the fluctuating density.

For b_{\parallel} and \mathbf{b}_{\perp} , we have

$$\frac{\partial \mathbf{B}_{\perp}}{\partial t} = -\frac{c}{4\pi en_e} \nabla_{\perp} \times [\mathbf{B} \cdot \nabla \mathbf{B}_{\parallel}], \quad (\text{A8})$$

$$\frac{\partial \mathbf{B}_{\parallel}}{\partial t} = -\mathbf{B}_0 \nabla \cdot \mathbf{v}_i - \frac{c}{4\pi en_e} \nabla_{\perp} \times [\mathbf{B} \cdot \nabla \mathbf{B}_{\perp}], \quad (\text{A9})$$

where we use $\nabla \times \approx \nabla_{\perp} \times$ and $\mathbf{B} \nabla \cdot \mathbf{v}_i = \mathbf{B}_0 \nabla \cdot \mathbf{v}_i + O(\epsilon^2)$. Here $\epsilon \sim k_{\parallel}/k_{\perp}$.

From the continuity equation, we can rewrite the $\mathbf{B}_0 \nabla \cdot \mathbf{v}_i (= \mathbf{B}_0 \nabla \cdot \mathbf{v}_e)$ as

$$\mathbf{B}_0 \nabla \cdot \mathbf{v}_i = -\mathbf{B}_0 \left(\frac{\partial}{\partial t} + \mathbf{v}_{\perp e} \cdot \nabla_{\perp} \right) \frac{\delta n_e}{n_e} \quad (\text{A10})$$

$$= \mathbf{B}_0 \left(\frac{\partial}{\partial t} + \mathbf{v}_{\perp e} \cdot \nabla_{\perp} \right) \frac{2}{\beta_i(1+Z/\tau)} \frac{b_{\parallel}}{B_0} \quad (\text{A11})$$

$$= \frac{2\hat{\mathbf{z}}}{\beta_i(1+Z/\tau)} \frac{\partial b_{\parallel}}{\partial t} + \frac{2}{\beta_i(1+Z/\tau)} \nabla_{\perp} \times (\mathbf{v}_{\perp e} \times b_{\parallel} \hat{\mathbf{z}}) \quad (\text{A12})$$

$$= \frac{2}{\beta_i(1+Z/\tau)} \frac{\partial \mathbf{b}_{\parallel}}{\partial t}, \quad (\text{A13})$$

where we use $\mathbf{b}_{\parallel} = b_{\parallel} \hat{\mathbf{z}}$, $\mathbf{v}_{\perp e} \times b_{\parallel} \hat{\mathbf{z}} = O(\epsilon^2) \approx 0$, and $b_{\parallel}/B_0 = -(\beta_i/2)(1+Z/\tau)(\delta n_e/n_e)$, which is equivalent to the pressure balance. Here, $Z = q_i/e$ ($e = |q_e|$) is the ion-to-electron charge ratio, $\tau = T_i/T_e$ is the temperature ratio, n_e is the mean electron number density, δn_e is the fluctuating electron number density, $\beta_i = 8\pi n_i k_B T_i / B_0^2$ is the ion plasma beta. Therefore, Eq. (A9) becomes

$$\frac{\partial \mathbf{B}_{\parallel}}{\partial t} = -\frac{\beta_i(1+Z/\tau)}{2+\beta_i(1+Z/\tau)} \frac{c}{4\pi en_e} \nabla_{\perp} \times [\mathbf{B} \cdot \nabla \mathbf{B}_{\perp}]. \quad (\text{A14})$$

In this paper, we use notations different from those in Schekochihin et al. (2009). The notations in this paper and in Schekochihin et al. (2009) are related by

$$\mathbf{b} \leftrightarrow \delta \mathbf{B}, \quad (\text{A15})$$

$$b_{\parallel} \leftrightarrow \delta B_{\parallel}, \quad (\text{A16})$$

$$\mathbf{b}_{\perp} \leftrightarrow \delta \mathbf{B}_{\perp} \quad (\text{A17})$$

$$n_e \leftrightarrow n_{0e}. \quad (\text{A18})$$

B. TWO-POINT SECOND-ORDER STRUCTURE FUNCTION AND SPECTRUM

We can obtain the 2-point second-order structure function of a variable A from $E_A(k)$:

$$SF_2(r) = \langle |A(\mathbf{x} + \mathbf{r}) - A(\mathbf{x})|^2 \rangle \quad (\text{B1})$$

$$= \int d^3 \mathbf{x} \int d^3 \mathbf{k} \hat{\mathbf{u}}(k) e^{i\mathbf{k} \cdot \mathbf{x}} (e^{i\mathbf{k} \cdot \mathbf{r}} - 1) \int d^3 \mathbf{k}' \hat{\mathbf{u}}(k') e^{i\mathbf{k}' \cdot \mathbf{x}} (e^{i\mathbf{k}' \cdot \mathbf{r}} - 1) \quad (\text{B2})$$

$$= \int d^3\mathbf{k} \hat{\mathbf{u}}(k) \hat{\mathbf{u}}^*(k) [2 - e^{i\mathbf{k}\cdot\mathbf{r}} - e^{-i\mathbf{k}\cdot\mathbf{r}}] \quad (\text{B3})$$

$$= 2\pi \int dk k^2 |\hat{\mathbf{u}}(k)|^2 \int d\theta \sin\theta [2 - e^{i\mathbf{k}\mathbf{r} \cos\theta} - e^{-i\mathbf{k}\mathbf{r} \cos\theta}] \quad (\text{B4})$$

$$= 8\pi \int dk k^2 |\hat{\mathbf{u}}(k)|^2 \left[1 - \frac{\sin kr}{kr}\right] \quad (\text{B5})$$

$$\propto 8\pi r^{m-1} \int_{k_0 r}^{\infty} d(kr) (kr)^{-m} \left[1 - \frac{\sin kr}{kr}\right], \quad (\text{B6})$$

where we assume

$$k^2 |\hat{\mathbf{u}}(k)|^2 \propto k^{-m} \quad (\text{B7})$$

for $k_0 < k < \infty$. In the limit of $kr \ll 1$, the integrand is proportional to $\sim (kr)^{2-m}$. Therefore, if $m < 3$, we can rewrite Eq. (B6) as

$$SF_2(r) \approx 8\pi r^{m-1} \int_0^{\infty} d(kr) (kr)^{-m} \left[1 - \frac{\sin kr}{kr}\right] \propto r^{m-1}. \quad (\text{B8})$$

If $m > 3$, however, the integral in Eq. (B6) is roughly proportional to $(k_0 r)(k_0 r)^{2-m} = (k_0 r)^{3-m}$ and we have

$$SF_2(r) \propto r^{m-1} (k_0 r)^{3-m} \propto r^2. \quad (\text{B9})$$

In summary, we have

$$SF_2(r) \propto \begin{cases} r^{m-1} & \text{if } m < 3 \\ r^2 & \text{if } m > 3. \end{cases} \quad (\text{B10})$$

In case of Kolmogorov, $m = 5/3 < 3$ and we have $SF_2(r) \propto r^{m-1} = r^{2/3}$. In case of EMHD, m for perpendicular direction ($m=7/3$) is still smaller than 3 and we have $SF_2(r) \propto r^{m-1} = r^{4/3}$. However, that for parallel direction is expected to be larger than 3 if turbulence is anisotropic. Therefore, the 2-point second-order structure function for parallel direction is not suitable for revealing the true scaling exponent and we will have $SF_2(r) \propto r^2$ for parallel direction.

C. MULTI-POINT SECOND-ORDER STRUCTURE FUNCTION AND SPECTRUM

Falcon et al. (2007) and Lazarian & Pogosyan (2008) used the 3-point second-order structure function that can work with a steeper $E(k)$:

$$SF_2(r) = \langle |A(\mathbf{x} + \mathbf{r}) - 2A(\mathbf{x}) + A(\mathbf{x} - \mathbf{r})|^2 \rangle \quad (\text{C1})$$

$$= \int d^3\mathbf{x} \int d^3\mathbf{k} \hat{\mathbf{u}}(k) e^{i\mathbf{k}\cdot\mathbf{x}} (e^{i\mathbf{k}\cdot\mathbf{r}} - 2 + e^{-i\mathbf{k}\cdot\mathbf{r}}) \int d^3\mathbf{k}' \hat{\mathbf{u}}(k') e^{i\mathbf{k}'\cdot\mathbf{x}} (e^{i\mathbf{k}'\cdot\mathbf{r}} - 2 + e^{-i\mathbf{k}'\cdot\mathbf{r}}) \quad (\text{C2})$$

$$= \int d^3\mathbf{k} \hat{\mathbf{u}}(k) \hat{\mathbf{u}}^*(k) [e^{i\mathbf{k}\cdot\mathbf{r}} - 2 + e^{-i\mathbf{k}\cdot\mathbf{r}}] [e^{i\mathbf{k}\cdot\mathbf{r}} - 2 + e^{-i\mathbf{k}\cdot\mathbf{r}}]^* \quad (\text{C3})$$

$$= 2\pi \int dk k^2 |\hat{\mathbf{u}}(k)|^2 \int d\theta \sin\theta [e^{2i\mathbf{k}\mathbf{r} \cos\theta} + e^{-2i\mathbf{k}\mathbf{r} \cos\theta} + 6 - 4e^{i\mathbf{k}\mathbf{r} \cos\theta} - 4e^{-i\mathbf{k}\mathbf{r} \cos\theta}] \quad (\text{C4})$$

$$= 8\pi \int dk k^2 |\hat{\mathbf{u}}(k)|^2 \left[\frac{\sin 2kr}{2kr} + 3 - 4 \frac{\sin kr}{kr} \right] \quad (\text{C5})$$

$$\propto 8\pi r^{m-1} \int_{k_0 r}^{\infty} d(kr) (kr)^{-m} \left[\left(4 - 4 \frac{\sin kr}{kr}\right) - \left(1 - \frac{\sin 2kr}{2kr}\right) \right], \quad (\text{C6})$$

where we assume $k^2 |\hat{\mathbf{u}}(k)|^2 \propto k^{-m}$ for $k_0 < k < \infty$. In the limit of $kr \ll 1$, the integrand is proportional to $\sim (kr)^{4-m}$. Therefore, the integral is roughly a constant (i.e. independent of r), if $m < 5$. If $m > 5$, however, the integral is roughly proportional to $(k_0 r)(k_0 r)^{4-m} = (k_0 r)^{5-m}$. Therefore, we have

$$SF_2(r) \propto \begin{cases} r^{m-1} & \text{if } m < 5 \\ r^{m-1} (k_0 r)^{5-m} \propto r^4 & \text{if } m > 5. \end{cases} \quad (\text{C7})$$

Similarly, we can construct a 4-point second-order structure function:

$$SF_2(r) = \langle |A(\mathbf{x} + 3\mathbf{r}) - 3A(\mathbf{x} + \mathbf{r}) + 3A(\mathbf{x} - \mathbf{r}) - A(\mathbf{x} - 3\mathbf{r})|^2 \rangle, \quad \text{or} \quad (\text{C8})$$

$$SF_2(r) = \langle |A(\mathbf{x} + \frac{3}{2}\mathbf{r}) - 3A(\mathbf{x} + \frac{1}{2}\mathbf{r}) + 3A(\mathbf{x} - \frac{1}{2}\mathbf{r}) - A(\mathbf{x} - \frac{3}{2}\mathbf{r})|^2 \rangle, \quad (\text{C9})$$

which scales as

$$SF_2(r) \propto \begin{cases} r^{m-1} & \text{if } m < 7 \\ r^{m-1} (k_0 r)^{7-m} \propto r^6 & \text{if } m > 7. \end{cases} \quad (\text{C10})$$

We can also construct a 5-point second-order structure function:

$$SF_2(r) = \langle |A(\mathbf{x} + 2\mathbf{r}) - 4A(\mathbf{x} + \mathbf{r}) + 6A(\mathbf{x}) - 4A(\mathbf{x} - \mathbf{r}) - A(\mathbf{x} - 2\mathbf{r})|^2 \rangle, \quad (\text{C11})$$

which scales as

$$SF_2(r) \propto \begin{cases} r^{m-1} & \text{if } m < 9 \\ r^{m-1} (k_0 r)^{9-m} \propto r^8 & \text{if } m > 9. \end{cases} \quad (\text{C12})$$